

Reconciliation of weak pairwise spike-train correlations and highly coherent local field potentials across space

Johanna Senk¹, Espen Hagen^{1,2}, Sacha J. van Albada¹, Markus Diesmann^{1,3,4}

¹Institute of Neuroscience and Medicine (INM-6) and Institute for Advanced Simulation (IAS-6) and JARA Institute Brain Structure-Function Relationships (INM-10), Jülich Research Centre, Jülich, Germany

²Department of Physics, University of Oslo, Oslo, Norway

³Department of Psychiatry, Psychotherapy and Psychosomatics, Medical Faculty, RWTH Aachen University, Aachen, Germany

⁴Department of Physics, Faculty 1, RWTH Aachen University, Aachen, Germany

Conflict of Interest

The authors declare no competing financial interests.

Acknowledgements

This project received funding from the European Union Seventh Framework Programme [FP7/2007-2013] under grant agreement No. 604102 (Human Brain Project, HBP), the European Union's Horizon 2020 research and innovation programme under grant agreement No. 720270 (HBP SGA1) and No. 785907 (HBP SGA2), the Helmholtz Association through the Helmholtz Portfolio Theme "Supercomputing and Modeling for the Human Brain", and the Research Council of Norway (NFR) through COBRA. The use of the supercomputer JURECA in Jülich was made possible by the JARA-HPC Vergabegremium and provided on the JARA-HPC Partition (VSR computation time grant JINB33).

We would like to thank Hans Ekkehard Plesser for helpful suggestions for the implementation of spatially structured networks in NEST, and Gaute T. Einevoll for providing useful feedback on the manuscript.

Abstract

Chronic and acute implants of multi-electrode arrays that cover several square millimeters of neural tissue provide simultaneous access to population signals such as extracellular potentials and the spiking activity of one hundred or more individual neurons. While the recorded data may uncover principles of brain function, its interpretation calls for multiscale computational models with corresponding spatial dimensions and signal predictions. Such models can then facilitate the search of candidate mechanisms underlying experimentally observed spatiotemporal activity patterns in cortex. Multi-layer spiking neuron network models of local cortical circuits covering about 1 mm^2 have been developed, integrating experimentally obtained neuron-type specific connectivity data and reproducing features of observed in-vivo spiking statistics. Using forward models, local field potentials (LFPs) can be computed from the simulated spiking activity. To account for the spatial scale of common neural recordings, we here extend a local network and LFP model to an area of $4 \times 4\text{ mm}^2$. The upscaling preserves the densities of neurons and local synapses, and introduces distance-dependent connection probabilities and conduction delays. As detailed experimental data on distance-dependent connectivity is partially lacking, we address this uncertainty in model parameters by testing different parameter combinations within biologically plausible bounds. Based on model predictions of spiking activity and LFPs, we find that the upscaling procedure preserves the overall spiking statistics of the original model and reproduces asynchronous irregular spiking across populations and weak pairwise spike-train correlations experimentally observed in sensory cortex. In contrast with the weak spike-train correlations, the correlation of LFP signals is strong and distance-dependent, compatible with experimental observations. Enhanced spatial coherence in the low-gamma band around 50 Hz may explain the recent experimental report of an apparent band-pass filter effect in the spatial reach of the LFP.

Significance Statement

Extracellular recordings with multi-electrode arrays measure both population signals such as the local field potential (LFP) and spiking activity of individual neurons across the cortical tissue, for instance covering the $4 \times 4\text{ mm}^2$ of a Utah array. To reproduce key features of activity data obtained from such cortical patches, we assess spiking activity and LFPs of a multiscale neuronal network model of this spatial extent. The circuit incorporates biological detail such as a realistic neuron density across four cortical layers and neuron-type-specific, layer-specific, and distance-dependent connection rules. The model reproduces experimental observations like a frequency-dependent LFP coherence across space despite weak pairwise spike-train correlations.

1 Introduction

Cortical activity on the mesoscopic scale (mesoscale), below a cortical surface area on the order of several square millimeters to centimeters (Muller et al., 2018), can be recorded extracellularly with chronic or acute implants of multi-electrode arrays (Maynard et al., 1997; Buzsáki et al., 2012; Einevoll et al., 2013a). The low-frequency part ($\lesssim 100\text{ Hz}$) of the measured extracellular potential, the local field potential (LFP), is a population signal with contributions from up to millions of local and remote neurons (Kajikawa and Schroeder, 2011; Lindén et al., 2011; Łęski et al., 2013). Spiking activity of individual neurons can be obtained from the high-frequency part ($\gtrsim 100\text{ Hz}$) of the signal through spike sorting (Quiroga, 2007). The number of reliably identified single neurons is on the order of 100 neurons for chronically implanted Utah arrays (10×10 electrodes on $4 \times 4\text{ mm}^2$, Blackrock microsystems, <http://blackrockmicro.com>) as in Riehle et al. (2013). The recordings expose LFP activity appearing to propagate across the cortex associated with distance dependency of statistical measures like correlations and coherences (Destexhe et al., 1999; Smith and Kohn, 2008; Wu et al., 2008; Muller and Destexhe, 2012; Sato et al., 2012; Dubey and Ray, 2016; Denker et al., 2018; Muller et al., 2018). The observation of coherent LFPs across space contrasts with the often reported low pairwise correlation in cortical spike trains obtained in asynchronous brain states (for example Ecker et al., 2010; Renart et al., 2010).

Assuming a neuron density of 10^5 neurons/ mm^2 across the cortical surface (Herculano-Houzel, 2009), the number of neurons covered by a Utah array is more than a million. Every neuron receives up to 10^4 synapses from neighboring and distant neurons (Abeles, 1991). However, the local circuitry is highly specific with respect to cortical layers and neuron types (Douglas et al., 1989; Thomson et al., 2002; Binzegger et al., 2004). The majority of local cortical connections are established within a distance of $\lesssim 500\ \mu\text{m}$ from the sender/receiving neuron (Voges et al., 2010), with probabilities that decay with distance according to a Gaussian or exponentially shaped profile (Hellwig, 2000; Boucsein et al., 2011; Packer and Yuste, 2011; Perin et al., 2011). Local connections are typically made by unmyelinated axons. Therefore, typical conduction delays between pre- and postsynaptic neurons are governed by propagation speeds estimated around 0.3 mm/ms (Hirsch and Gilbert, 1991; Murakoshi et al., 1993; Kang et al., 1994).

To date, the relationship between cortical connectivity structure and experimentally recorded activity of spikes and LFPs on the mesoscale remains poorly understood. Network models that encompass the relevant anatomical and physiological detail, spatial scales, and corresponding measurements can aid the interpretation of experimental

observations and their underlying mechanisms. We here argue for full-scale models, in terms of realistic numbers of neurons and synapses: Downscaled or diluted network models may not reproduce first- and second-order statistics (rates and correlations, respectively) of full-scale networks (van Albada et al., 2015). Also, Hagen et al. (2016) demonstrate that biophysical forward-model predictions of LFP signals (and by extension electroencephalographic (EEG) and magnetoencephalographic (MEG) signals) must include the full density of cells and connections to account for network correlations. One such full-density model, the microcircuit model by Potjans and Diesmann (2014), represents a 1 mm^2 cortical patch of early sensory cortex with approximately 80,000 leaky integrate-and-fire neurons and about 0.3 billion synapses set up using neuron-type- and layer-specific connection probabilities derived from anatomical and electrophysiological data. This model produces biologically plausible firing rates across four cortical layers with one excitatory and inhibitory population per layer, is simple enough to allow for rigorous mathematical analysis, is publicly available, and has by now been used also in other studies (Wagatsuma et al., 2011; Bos et al., 2016; Cain et al., 2016; Hagen et al., 2016; Hahne et al., 2017; Senk et al., 2017; Schuecker et al., 2017; Schwalger et al., 2017; Schmidt et al., 2018; van Albada et al., 2018).

Here, we hypothesize that a version of this microcircuit model and corresponding LFP measurements upscaled laterally to an area of at least $4 \times 4 \text{ mm}^2$ (similar to the Utah multi-electrode array), while accounting for distance-dependent connection probabilities, should not only preserve the main features of activity in the original model, but also explain features emerging on the mesoscale such as spatial propagation of evoked neuronal activity (Bringuier et al., 1999; Swadlow et al., 2002; Einevoll et al., 2007; Muller et al., 2014; Klein et al., 2016), and strong distance-dependent correlations and coherences in the measured LFP (Destexhe et al., 1999; Berens et al., 2008; Katzner et al., 2009; Nauhaus et al., 2009; Kajikawa and Schroeder, 2011; Jia et al., 2011; Srinath and Ray, 2014; Dubey and Ray, 2016) even for typically weak pairwise spike-train correlations in cortex (see, for example, Ecker et al., 2010; Renart et al., 2010). Furthermore, the upscaled model should serve as a test platform for parameters that are to date poorly constrained by available experimental data, and expose mechanisms underlying spatiotemporal pattern formation. Indeed, we find that the overall behavior of the original microcircuit is preserved when upscaled, and that the resulting model reconciles the observation of weak pairwise spike-train correlations in cortex with spatially correlated and coherent LFPs.

Preliminary results have been published in abstract form (Senk et al., 2015; Hagen et al., 2016).

2 Materials and Methods

2.1 Point-neuron networks

This section provides a compact description of the different network models considered in this study. The full network descriptions are given in Tables 1 and 2. Each network model represents a part of early sensory cortex with realistic densities of neurons and synapses. We first consider the original network model proposed by Potjans and Diesmann (2014) which describes a microcircuit under 1 mm^2 cortical surface, henceforth referred to as ‘reference model’. We then consider networks upscaled to greater surface areas, referred to as ‘upscaled models’. The eight neuron populations within each network are organized into four cortical layers, that is, layer 2/3 (L2/3), layer 4 (L4), layer 5 (L5) and layer 6 (L6), respectively. Each layer contains an excitatory (E) and an inhibitory (I) population of leaky integrate-and-fire (LIF) neurons, whose sub-threshold membrane dynamics are governed by Equation 13. The probabilities for two neurons to be connected are layer- and neuron-type-specific and derived from a number of anatomical and electrophysiological studies (Potjans and Diesmann, 2014). Postsynaptic currents have static, normally distributed amplitudes at onset that decay exponentially (Equations 14 and 15). All neurons receive stationary external input in the form of Poisson spike trains with fixed rate parameters. In addition, one population of thalamocortical (TC) neurons targeting E and I neurons in both L4 and L6 can provide transient or stationary external input, for example to emulate stimuli of the sensory pathway.

2.1.1 Network model descriptions

We here describe the main differences between the original network model and upscaled models derived from it.

Reference model: Potjans and Diesmann (2014) parameterize the original microcircuit model to cover a cortical column under a surface area of $A^r = 1 \text{ mm}^2$. The superscript r denotes ‘reference model’ here and throughout this manuscript. The resulting network connects almost 80,000 neurons with approximately 0.3 billion synapses. The calculation of connection probabilities in the model assumes a Gaussian distance dependency of the form (see Potjans and Diesmann (2014) for details)

$$c^r(r) = c_0 e^{-r^2/2\sigma_0^2}. \quad (1)$$

Here, r denotes the lateral distance between the two neurons. This distance dependency is introduced to reconcile connectivity measurements obtained using anatomical connectivity data (retrograde/anterograde staining, Binzegger et al., 2004) and electrophysiological data (in vitro, Thomson et al., 2002). The computed mean values averaged over all populations for zero-distance connection probability and standard deviation are $c_0 = 0.14$ and $\sigma_0 = 0.30 \text{ mm}$,

respectively (Potjans and Diesmann, 2014, Equations 4-8, Figure 3). This spatial decay constant is large compared to the extent of a typical cortical column, which justifies their choice of a local network connectivity without distance dependency.

A neuron j in a source population X of size N_X^r connects at random to a neuron i in a target population Y of size N_Y^r with mean connection probability (Potjans and Diesmann, 2014, Equation 1)

$$C_{YX}^r = 1 - \left(1 - \frac{1}{N_X^r N_Y^r}\right)^{S_{YX}^r}, \quad (2)$$

where S_{YX}^r denotes the total number of synapses between these populations. The connection routine draws connections randomly between pairs of neurons i and j until the total number of synapses S_{YX}^r is reached. Multiple connections (multapses) between neuron pairs are allowed. The connection probability C_{YX}^r is here defined as the probability that a pair of neurons is connected via one or more synapses. Connection delays are normally distributed according to Equation 17 with different parameters for excitatory and inhibitory sources. The standard deviation of delays is 50% of the mean delay, and the excitatory mean delay is twice as long as the inhibitory one.

Upscaled models: We next consider cortical network models based on the reference network upscaled to cover an area of $A^u = L^2$. With square layers and a chosen side length $L = 4$ mm this area is similar to the area covered by the Utah array (10×10 electrodes, Blackrock Microsystems). The superscript u denotes ‘upscaled models’ here and throughout this manuscript. In the upscaled models, neuron positions are drawn randomly within a square domain of side length L with the origin $(0,0)$ at the center. We position neurons in the TC layer also within the area A^u , which facilitates the connectivity management between TC neurons and cortical neurons in the model. An analogy to the early visual pathway would be that the distance L in both thalamus and cortex corresponds to the same extent of the visual field. A source neuron $j \in X$ at location (x_j, y_j) connects to a target neuron $i \in Y$ at location (x_i, y_i) with a probability dependent on their distance r_{ij} given in Equation 11. This expression for distance accounts for periodic boundary conditions (torus connectivity). The distance-dependent connection probability is shaped as a two-dimensional (2D) Gaussian and cut off at a maximal radial distance R as defined in Equation 12. The zero-distance connection probability c_{YX} between populations X and Y is derived in Section 2.1.2. The corresponding standard deviation σ_X defines the spatial width of the profile and depends only on the source population X . Connection delays of the upscaled models are calculated using a linear distance dependency given by Equation 18 with a constant delay offset d_0 and a conduction speed v , plus a random offset drawn from a normal distribution with zero mean and standard deviation σ_d^u capped at values $\pm(d_0 - dt)$ in order to prevent delays smaller than the simulation time step dt . These values are the same for all cortical populations. For the external layer, TC neurons within a circle of adjustable radius $R_{\text{pulse}}^{\text{TC}}$ surrounding the center emit spikes in a synchronous and regular fashion (thalamic pulses) with time intervals Δt_{TC} .

These network model implementations rely on the neuronal network simulator NEST (<http://www.nest-simulator.org>, Gewaltig and Diesmann, 2007) and are set up such that the same code is used for both the reference and upscaled models, but with different parameters.

2.1.2 Upscaling procedure

We here describe the procedure used to derive parameters for the upscaled model(s) from the original reference network model description, in terms of neuron numbers, synapse numbers, distance-dependent connection probabilities, in-degrees of external input, and distance-dependent delays from available experimental data.

Neuron numbers: The upscaled networks preserve the neuron densities per square millimeter of the reference model. Assuming a homogeneous neuron density across space, the size of a population X in the upscaled networks is

$$N_X^u = N_X^r \frac{A^u}{A^r}. \quad (3)$$

Synapse numbers: With the aim to derive zero-distance connection probabilities c_{YX} for a Gaussian connectivity profile Equation 12, we first compute average connection probabilities C_{YX}^u in the upscaled models similar to C_{YX}^r for the reference model (as in Equation 2, but with corresponding neuron and synapse numbers). We define this connection probability as

$$C_{YX}^u = C_{YX}^{\text{ui}} \cdot (1 - \delta C_{YX}). \quad (4)$$

The superscript ui denotes upscaled, intermediate connection probabilities. The term δC_{YX} is introduced to allow for selective modifications of the connection probabilities in the final upscaled network (for example to modify firing rate spectra, see below). Thus, connections are unchanged for $\delta C_{YX} = 0$, meaning $C_{YX}^u = C_{YX}^{\text{ui}}$, but a small positive or negative value results in an increase or decrease of a specific connection probability between populations X and Y , respectively. The connection probability C_{YX}^{ui} depends linearly on the corresponding population-specific connection probability of the reference model, C_{YX}^r , and the ratio of mean connection probabilities from the upscaled and reference models (Schmidt et al., 2018, Equation 6)

$$C_{YX}^{\text{ui}} = C_{YX}^{\text{r}} \frac{\bar{C}^{\text{u}}}{\bar{C}^{\text{r}}}. \quad (5)$$

Like Schmidt et al. (2018), we choose to use the average connection probability of the reference model $\bar{C}^{\text{r}} = 0.066$ as computed in (Potjans and Diesmann, 2014, Equation 9). To compute the average connection probability \bar{C}^{u} of the upscaled models, we integrate the Gaussian profile given in Equation 1 over all possible positions of a source neuron (x_1, y_1) and a target neuron (x_2, y_2) , located on a square domain of side length L . Accounting for the maximal radial distance of connections, set to $R = L/2$, and the periodic boundary conditions used for the upscaled model, we numerically solve

$$\bar{C}^{\text{u}} = \frac{1}{L^4} \int_{-L/2}^{L/2} \int_{-L/2}^{L/2} \int_{x_1-L/2}^{x_1+L/2} \int_{y_1-L/2}^{y_1+L/2} c^{\text{r}}(r_{21}) dy_2 dx_2 dy_1 dx_1 \quad (6)$$

where $r_{21} = \sqrt{(x_2 - x_1)^2 + (y_2 - y_1)^2}$ with c^{r} as defined in Equation 1.

The total number of synapses S_{YX}^{u} follows from Equation 2, using connection probabilities and neuron numbers from the upscaled models. This in turn yields the average number of incoming connections to the target neurons, the synaptic in-degree, as $K_{YX}^{\text{u}} = S_{YX}^{\text{u}}/N_Y^{\text{u}}$. Connections in the upscaled model are drawn at random according to the spatial profile (Equation 12) and we fix only the zero-distance connection probability c_{YX} and the spatial width σ_X , such that the upscaled in-degree K_{YX}^{u} is achieved. Under the assumption of a homogeneous distribution of neurons and connections inside a disc with radius R around a target neuron, the local connection probability is then $c_{YX,R} = K_{YX}^{\text{u}}/N_{X,R}^{\text{u}}$, where $N_{X,R}^{\text{u}}$ denotes the number of potential source neurons. We eliminate $N_{X,R}^{\text{u}}$ from the expression for $c_{YX,R}$ by relating neuron numbers to surface areas: $N_{X,R}^{\text{u}} = N_X^{\text{u}} \cdot A_R/A^{\text{u}}$ with $A_R = \pi R^2$ and $A^{\text{u}} = L^2$. To achieve the same in-degree for the uniform connection probability $c(r) = c_{YX,R} \Theta(R - r)$ and the distance-dependent connection probability (Equation 12), the following volume integral in polar coordinates must be equal for both choices of $c(r)$: $\int_0^{2\pi} \int_0^\infty \int_0^{c(r)} r dz dr d\varphi$. Due to isotropy, it is enough to equate $\int_0^\infty r c(r) dr$ for both connection probabilities to derive the zero-distance connection probability of the distance-dependent profile,

$$c_{YX} = \frac{K_{YX}^{\text{u}} L^2}{2\pi \sigma_X^2 N_X^{\text{u}} \left[1 - \exp\left(-\frac{R^2}{2\sigma_X^2}\right) \right]}. \quad (7)$$

The connection routine used for the upscaled models does not fix the total number of synapses, unlike the routine used for the reference model. Each pair of neurons is considered only once in contrast to the reference model which samples the neurons with replacement. If $c_{YX} > 1$, the routine is executed N_c times with zero-distance connection probabilities c_{YX}/N_c where $N_c = \lceil c_{YX} \rceil$. In this case, a pair of neurons can be connected by up to N_c synapses.

Mean input: To preserve the mean input to each neuron of the reference network in the upscaled network, we adjust the in-degrees of the external stationary Poisson input to compensate for differences in internal in-degrees between the reference and the upscaled model that result from the above calculation of recurrent synaptic in-degrees. If the mean connection weight $g_{YX} \cdot J$ for internal connections, the weight for external input J , the population firing rates ν_X , and the external Poisson rate ν_{ext} are the same for both models, the external in-degrees $K_{Y,\text{ext}}^{\text{u}}$ per population Y of the upscaled model follow from the external in-degrees of the reference model $K_{Y,\text{ext}}^{\text{r}}$ and the difference in internal in-degrees:

$$\begin{aligned} \sum_X K_{YX}^{\text{u}} g_{YX} \nu_X + K_{Y,\text{ext}}^{\text{u}} \nu_{\text{ext}} &= \sum_X K_{YX}^{\text{r}} g_{YX} \nu_X + K_{Y,\text{ext}}^{\text{r}} \nu_{\text{ext}} \\ K_{Y,\text{ext}}^{\text{u}} &= K_{Y,\text{ext}}^{\text{r}} + \sum_X \frac{g_{YX} \nu_X}{\nu_{\text{ext}}} (K_{YX}^{\text{r}} - K_{YX}^{\text{u}}). \end{aligned} \quad (8)$$

This modification of external in-degrees in the upscaled network only preserves the mean of the spiking input (which is proportional to both in-degrees and weights), but not its variance (which is proportional to in-degrees and to weights squared); see, for example, Brunel and Hakim (1999); van Albada et al. (2015) for details.

Delays: To compare the mean delays of the reference model (Equation 17) and mean delays resulting from linear distance dependency in the upscaled model (Equation 18), we compute an effective delay for the upscaled model. The effective delay is computed as the average delay of the distance-dependent version evaluated on a disc of 1 mm^2 (with radius $Q = 1/\sqrt{\pi} \text{ mm}$), thus equalling the extent of the reference model. Accounting for all distances between random points on the disc, the effective delay in polar coordinates for a disc of radius Q is

$$\bar{d}_Q(\sigma_X) = \frac{1}{\pi^2 Q^4} \int_0^Q \int_0^{2\pi} \int_0^Q \int_0^{2\pi} \left(d_0 + \frac{r_{21}}{v} \right) \frac{1}{c_{\text{norm}}} e^{-\frac{r_{21}^2}{2\sigma_X^2}} r_1 r_2 d\varphi_1 dr_1 d\varphi_2 dr_2 \quad (9)$$

with $r_{21} = r_1^2 + r_2^2 - 2r_1r_2\cos(\varphi_1 - \varphi_2)$. We here account for the Gaussian distance dependency of the spatial profile Equation 12 with spatial width σ_X but normalize the profile to unity for the integral over the disc by the factor c_{norm} , and ignore the Heaviside function because we only consider $Q < R$. The expression simplifies (Sheng, 1985, Theorem 2.4) to

$$\bar{d}_Q(\sigma_X) = \frac{\int_0^{2Q} [d_0 + \frac{r}{v}] \exp\left(-\frac{r^2}{2\sigma_X^2}\right) r \left[4 \arctan\left(\sqrt{\frac{2Q-r}{2Q+r}}\right) - \sin\left(4 \arctan\left(\sqrt{\frac{2Q-r}{2Q+r}}\right)\right)\right] dr}{\int_0^{2Q} \exp\left(-\frac{r^2}{2\sigma_X^2}\right) r \left[4 \arctan\left(\sqrt{\frac{2Q-r}{2Q+r}}\right) - \sin\left(4 \arctan\left(\sqrt{\frac{2Q-r}{2Q+r}}\right)\right)\right] dr}, \quad (10)$$

which we evaluate numerically. Hence, the delay offset d_0 and conduction speed v can be set based on available experimental data, and the mean delays in the upscaled network can be compared with the corresponding excitatory and inhibitory mean delays of the reference model.

2.2 Forward modeling of extracellular potentials

In the present study we use a now well-established method to compute extracellular potentials from neuronal activity. The method relies on multicompartment neuron modeling to compute transmembrane currents (see, for example, De Schutter and Van Geit, 2009) and volume conduction theory (Nunez and Srinivasan, 2006; Einevoll et al., 2013b) which relates current sources and electric potentials in space. Assuming a volume conductor model that is linear (frequency-independent), homogeneous (the same in all locations), isotropic (the same in all directions), and ohmic (currents depend linearly on the electric field \mathbf{E}), as represented by the scalar electric conductivity σ_e , the electric potential in location $\mathbf{r} \equiv (x, y, z)$ of a time-varying point current with magnitude $I(t)$ in location \mathbf{r}' is given by

$$\phi(\mathbf{r}, t) = \frac{I(t)}{4\pi\sigma_e|\mathbf{r} - \mathbf{r}'|}. \quad (19)$$

The potential is assumed to be measured relative to an ideal reference at infinite distance from the source. Consider a set of transmembrane currents of n_{comp} individual cylindrical compartments indexed by n in an N -sized population of cells indexed by j with time-varying magnitude $I_{jn}^m(t)$ embedded in a volume conductor representing the surrounding neural tissue. The extracellular electric potential is then calculated as the linear sum

$$\phi(\mathbf{r}, t) = \sum_{j=1}^N \sum_{n=1}^{n_{\text{comp}}} \frac{I_{jn}^m(t)}{4\pi\sigma_e} \int \frac{1}{|\mathbf{r} - \mathbf{r}_{jn}|} d\mathbf{r}_{jn}. \quad (20)$$

The integral term here enters as we utilize the *line-source* approximation (Holt and Koch, 1999) which amounts to assuming a homogeneous transmembrane current density per unit length and integrating Equation 19 along the center axis of each cylindrical compartment. The thick soma compartments (with $n = 1$) with magnitude $I_j^{\text{m,soma}}(t)$, however, are approximated as spherical current sources, which amounts to combining Equations 19 and 20 as Lindén et al. (2014)

$$\begin{aligned} \phi(\mathbf{r}, t) &= \sum_{j=1}^N \frac{1}{4\pi\sigma_e} \left(\frac{I_j^{\text{m,soma}}(t)}{|\mathbf{r} - \mathbf{r}_j^{\text{soma}}|} + \sum_{n=2}^{n_{\text{comp}}} \int \frac{I_{jn}^m(t)}{|\mathbf{r} - \mathbf{r}_{jn}|} d\mathbf{r}_{jn} \right) \\ &= \sum_{j=1}^N \frac{1}{4\pi\sigma_e} \left(\frac{I_j^{\text{m,soma}}(t)}{|\mathbf{r} - \mathbf{r}_j^{\text{soma}}|} + \sum_{n=2}^{n_{\text{comp}}} \frac{I_{jn}^m(t)}{\Delta s_{jn}} \ln \left| \frac{\sqrt{h_{jn}^2 + r_{\perp jn}^2} - h_{jn}}{\sqrt{l_{jn}^2 + r_{\perp jn}^2} - l_{jn}} \right| \right). \end{aligned} \quad (21)$$

Here, lengths of compartments n of cells j are denoted by Δs_{jn} , perpendicular distances from the electrode point contact to the axis of the line compartments by $r_{\perp jn}$, and longitudinal distances measured from the start of the compartment by h_{jn} . The distances $l_{jn} = \Delta s_{jn} + h_{jn}$ are measured longitudinally from the end of the compartment. As the above denominators can be arbitrarily small and cause singularities in the computed extracellular potential, we set the minimum separation $|\mathbf{r} - \mathbf{r}_j^{\text{soma}}|$ or $r_{\perp jn}$ equal to the radius of the corresponding compartment.

The above equations assume point electrode contacts, while real electrode contacts have finite extents. We employ the *disc-electrode* approximation (Camuñas Mesa and Quiroga, 2013; Lindén et al., 2014; Ness et al., 2015)

$$\phi_{\text{disc}}(\mathbf{u}, t) = \frac{1}{A_S} \iint_S \phi(\mathbf{u}, t) d^2r \approx \frac{1}{m} \sum_{h=1}^m \phi(\mathbf{u}_h, t) \quad (22)$$

to approximate the averaged potential across the uninsulated contact surface (Robinson, 1968; Nelson et al., 2008; Nelson and Pouget, 2010; Ness et al., 2015). We average the potential (Equation 21) in $m = 50$ randomized locations \mathbf{u}_h on each circular and flat contact surface S with surface area A_S and radius $5 \mu\text{m}$. The surface normal vector on the disc representing each contact is the unit vector along the vertical z -axis. All forward-model calculations are performed with the simulation tool LFPy (<https://lfp.readthedocs.io>, Lindén et al., 2014; Hagen et al., 2018), which uses the NEURON simulation software (<https://neuron.yale.edu>, Carnevale and Hines, 2006; Hines et al., 2009) to calculate transmembrane currents.

A: Model summary	
Structure	Multi-layer excitatory-inhibitory (E-I) network
Populations	8 cortical in 4 layers (L2/3, L4, L5, L6) and 1 thalamic (TC)
Input	Cortex: Independent fixed-rate Poisson spike trains to all neurons (population-specific in-degree)
Measurements	Spikes, LFP, CSD, MUA
Neuron model	Cortex: leaky integrate-and-fire (LIF); Thalamus: point process
Synapse model	Exponentially shaped postsynaptic currents with normally distributed static weights
Reference model	
Topology	None (no spatial information)
Delay model	Normally distributed delays
Connectivity	Random, independent, population-specific, fixed number of synapses
Upscaled models	
Topology	Random neuron positions on square domain of size $L \times L$; periodic boundary conditions
Delay model	Distributed distance-dependent delays
Connectivity	Random, distance-dependent connection probability, population-specific, number of synapses not fixed in advance
B: Network models	
Connectivity	Connection probabilities C_{YX} from population X to population Y with $\{X, Y\} \in \{L2/3, L4, L5, L6\} \times \{E, I\} \cup TC$, $C_{YX} = 0$ for $Y = TC$
	Reference model
	Fixed number of synapses S_{YX} between populations X and Y (see Equation 2), binomially distributed in-/out-degrees
	Upscaled models
	<ul style="list-style-type: none"> • Presynaptic neuron $j \in X$ at location (x_j, y_j) and postsynaptic neuron $i \in Y$ at (x_i, y_i) • Neuron inter-distance (periodic boundary conditions): $r_{ij} = \sqrt{\Delta x_{ij}^2 + \Delta y_{ij}^2} \quad (11)$ with $\Delta x_{ij} = x_i - x_j$ if $x_i - x_j \leq L/2$, otherwise $\Delta x_{ij} = L - x_i - x_j$ (same for Δy_{ij}) • Gaussian-shaped connection probability with maximal distance R, spatial width σ_X and zero-distance connection probability c_{YX} (see Equation 7): $c^u(r_{ij}) = c_{YX} e^{-r^2/2\sigma_X^2} \Theta(R - r_{ij}) \quad (12)$ Heaviside function $\Theta(t) = 1$ for $t \geq 0$, and 0 otherwise.

Table 1: **Description of reference and upscaled network models following the guidelines of Nordlie et al. (2009).**

C: Neuron models	
Cortex	Leaky integrate-and-fire neuron (LIF) <ul style="list-style-type: none"> • Dynamics of membrane potential $V_i(t)$ for neuron i: <ul style="list-style-type: none"> – Spike emission at times t_s^i with $V_i(t_s^i) \geq V_\theta$ – Subthreshold dynamics: $\tau_m \dot{V}_i = -V_i + R_m I_i(t) \quad \text{if } \forall s : t \notin (t_s^i, t_s^i + \tau_{\text{ref}}] \quad \text{with } \tau_m = R_m C_m \quad (13)$ – Reset + refractoriness: $V_i(t) = V_{\text{reset}}$ if $\forall s : t \in (t_s^i, t_s^i + \tau_{\text{ref}}]$ • Exact integration with temporal resolution dt (Rotter and Diesmann, 1999) • Random, uniform distribution of membrane potentials at $t = 0$
Thalamus	Spontaneous activity: no thalamic input ($\nu_{\text{TC}} = 0$)
Upscaled models	
Thalamus	Thalamic pulses: coherent activation of all thalamic neurons inside a circle with radius $R_{\text{TC}}^{\text{pulse}}$ centered around $(0,0)$ at fixed time intervals Δt_{TC}
D: Synapse models	
Postsynaptic currents	<ul style="list-style-type: none"> • Instantaneous onset, exponentially decaying postsynaptic currents • Input current of neuron i from presynaptic neuron j: $I_i(t) = \sum_j J_{ij} \sum_s e^{-(t-t_s^j-d_{ij})/\tau_s} \Theta(t-t_s^j-d_{ij}) \quad (14)$
Weights	<ul style="list-style-type: none"> • Normal distribution with static weights, clipped to preserve sign: $J_{ij} \sim \mathcal{N}\{\mu = g_{YX} \cdot J, \sigma^2 = \sigma_{J,YX}^2\} \quad (15)$ • Probability density of normal distribution: $f(x \mu, \sigma^2) = \frac{1}{\sqrt{2\pi\sigma^2}} e^{-\frac{(x-\mu)^2}{2\sigma^2}} \quad (16)$
Reference model	
Delays	Normal distribution, left-clipped at dt : $d_{ij} = d_{ij}^r \sim \mathcal{N}\{\mu = \bar{d}_X, \sigma^2 = (\sigma_{d,X}^r)^2\} \quad (17)$
Upscaled models	
Delays	Linear distance dependency with delay offset d_0 and conduction speed v . Normally distributed additive noise, left-clipped at $-(d_0 - dt)$ and right-clipped at $d_0 - dt$: $d_{ij} = d_{ij}^u \sim d_0 + \frac{r_{ij}}{v} + \mathcal{N}\{\mu = 0, \sigma^2 = (\sigma_d^u)^2\} \quad (18)$

Table 2: Description of reference and upscaled network models (continuation of Table 1).

A: Global simulation parameters		
Symbol	Value	Description
T_{sim}	5,000 ms	Simulation duration
dt	0.1 ms	Temporal resolution
T_{trans}	500 ms	Startup transient
B: Preprocessing		
Symbol	Value	Description
Δt	0.5 ms	Temporal bin size
Δl	0.1 mm	Spatial bin size
C: Global network parameters		
Connection parameters and external input		
Symbol	Value	Description
J	87.81 pA	Reference synaptic strength. All synapse weights are measured in units of J .
g_{YX}	1	Relative synaptic strengths: $X \in \{\text{L2/3E, L4E, L5E, L6E, TC}\}$
	-4	$X \in \{\text{L2/3I, L4I, L5I, L6I}\}$, except for:
	2	$(X, Y) = (\text{L4E, L2/3E})$
$\sigma_{J,YX}$	$0.1 \cdot g_{YX} \cdot J$	Standard deviation of weight distribution
ν_{ext}	8 s^{-1}	Rate of external input with Poisson inter-spike interval statistics
LIF neuron model		
Symbol	Value	Description
C_m	250 pF	Membrane capacitance
τ_m	10 ms	Membrane time constant
E_L	-65 mV	Resistive leak reversal potential
V_θ	-50 mV	Spike detection threshold
V_{reset}	-65 mV	Spike reset potential
τ_{ref}	2 ms	Absolute refractory period after spikes
τ_s	0.5 ms	Postsynaptic current time constant

Table 3: Global simulation, preprocessing, and network parameters used for both reference and upscaled network models.

Additional network parameters for reference model										
Populations and external input										
Symbol	Value									Description
X	L2/3E	L2/3I	L4E	L4I	L5E	L5I	L6E	L6I	TC	Name
N_X^r	20,683	5,834	21,915	5,479	4,850	1,065	14,395	2,948	902	Size
$K_{X,\text{ext}}^r$	1,600	1,500	2,100	1,900	2,000	1,900	2,900	2,100	-	External in-degree
Connection probabilities										
C_{YX}^r	from X									
		L2/3E	L2/3I	L4E	L4I	L5E	L5I	L6E	L6I	TC
	L2/3E	0.1009	0.1689	0.0437	0.0818	0.0323	0.0	0.0076	0.0	0.0
	L2/3I	0.1346	0.1371	0.0316	0.0515	0.0755	0.0	0.0042	0.0	0.0
	L4E	0.0077	0.0059	0.0497	0.1350	0.0067	0.0003	0.0453	0.0	0.0983
	L4I	0.0691	0.0029	0.0794	0.1597	0.0033	0.0	0.1057	0.0	0.0619
	L5E	0.1004	0.0622	0.0505	0.0057	0.0831	0.3726	0.0204	0.0	0.0
	L5I	0.0548	0.0269	0.0257	0.0022	0.0600	0.3158	0.0086	0.0	0.0
	L6E	0.0156	0.0066	0.0211	0.0166	0.0572	0.0197	0.0396	0.2252	0.0512
L6I	0.0364	0.0010	0.0034	0.0005	0.0277	0.0080	0.0658	0.1443	0.0196	
to Y										
Connection Parameters										
Symbol	Value									Description
\bar{d}_E	1.5 mm									Mean excitatory delay
\bar{d}_I	0.75 mm									Mean inhibitory delay
$\sigma_{\bar{d},X}^r$	$0.5 \cdot \bar{d}_X$									Standard deviation of delay distribution

Table 4: Additional network parameters for the reference model.

Additional network parameters for the final upscaled model										
Populations and external input										
Symbol	Value									Description
X	L2/3E	L2/3I	L4E	L4I	L5E	L5I	L6E	L6I	TC	Name
N_X^u	330,928	93,344	350,640	87,664	77,600	17,040	230,320	47,168	14,432	Size
$K_{X,\text{ext}}^u$	1,702	1,621	1,864	2,443	1,939	1,724	3,051	2,246	-	External in-degree
Connection probabilities										
C_{YX}^u to Y	from X									
		L2/3E	L2/3I	L4E	L4I	L5E	L5I	L6E	L6I	TC
	L2/3E	0.007540	0.012622	0.003266	0.006113	0.002414	0.0	0.000568	0.0	0.0
	L2/3I	0.010059	0.010245	0.002361	0.003849	0.005642	0.0	0.000314	0.0	0.0
	L4E	0.000575	0.000441	0.003714	0.008575	0.000501	0.000022	0.003385	0.0	0.007346
	L4I	0.005164	0.000217	0.005934	0.013725	0.000247	0.0	0.007899	0.0	0.004626
	L5E	0.007503	0.004648	0.003774	0.000426	0.006210	0.029237	0.001524	0.0	0.0
	L5I	0.004095	0.002010	0.001921	0.000164	0.003587	0.021240	0.000643	0.0	0.0
	L6E	0.001166	0.000493	0.001577	0.001241	0.004275	0.001472	0.002959	0.016829	0.003826
	L6I	0.002720	0.000075	0.000254	0.000037	0.002070	0.000598	0.004917	0.010784	0.001465
Connection probability modifications										
Symbol	Value		Description							
δC_{YX}	0		$\{X, Y\} \in \{\text{L2/3E, L2/3I, L4E, L4I, L5E, L5I, L6E, L6I, TC}\}$, except for:							
	-0.15		$(X, Y) = (\text{L4I, L4E})$							
	0.15		$(X, Y) = (\text{L4I, L4I})$							
	-0.2		$(X, Y) = (\text{L5E, L5I})$							
	0.05		$(X, Y) = (\text{L5I, L5E})$							
	-0.1		$(X, Y) = (\text{L5I, L5I})$							
Connection Parameters										
Symbol	Value		Description							
d_0	0.5 ms		Delay offset							
v	0.3 mm/ms		Conduction speed							
σ_d^u	0.1 ms		Width of jitter distribution for delay							
σ_E	0.35 mm		Excitatory spatial width							
σ_I	0.1 mm		Inhibitory spatial width							
Thalamus										
Symbol	Value		Description							
$R_{\text{TC}}^{\text{pulse}}$	0.3 mm		TC neuron activation radius of disc around (0,0), all TC neurons in the disc are active during pulses							
σ_{TC}	0.3 mm		Spatial width of TC neuron connections							
Δt_{TC}	100 ms		Interval between thalamic pulses							

Table 5: Additional network parameters for the final upscaled model.

2.2.1 Modifications to the hybrid scheme

Extracellular potentials from the point-neuron network models are here calculated using a slightly modified version of the biophysics-based hybrid scheme introduced by Hagen et al. (2016). The scheme combines forward modeling of extracellular potentials, or more specifically its low-frequency part termed the local field potential (LFP), from spatially extended multicompartment neuron models described above instead of point neurons. Point neurons cannot generate an extracellular potential, as the sum of all in- and outgoing currents vanishes in a point, in contrast to multicompartment neuron models, which can account for in- and outgoing currents distributed in space. We refer the reader to the Methods of Hagen et al. (2016) for an in-depth technical description of the implementation for randomly connected point-neuron network models. Here, we only summarize its main steps and list the main changes which allow accounting for extracellular potentials of networks with distance-dependent connectivity and periodic boundary conditions. This hybrid modeling scheme for extracellular potentials combines the simplicity and efficiency of point-neuron network models with multicompartment neuron models for LFP generation accounting for the biophysical origin of extracellular potentials. As in Hagen et al. (2016), we assume that cortical network dynamics are well captured by the point-neuron network, and implement the hybrid scheme as follows:

- Spike trains of individual point neurons are mapped to synapse activation times on corresponding postsynaptic multicompartment neurons while overall connection parameters are preserved, that is, the distribution of delays, the mean postsynaptic currents, and the mean number of incoming connections onto individual cells (in-degree).
- Each multicompartment neuron has its equivalent in the point-neuron network and receives input spikes from presynaptic point neurons with the same distribution as in the point-neuron network (the mean in-degree of neurons in the network and the cell-type and layer specificity of connections is preserved, as in Hagen et al. (2016)).
- The multicompartment neurons are mutually unconnected, and synaptic activations are translated into a distribution of transmembrane currents that contributes to the total LFP.
- Activity in multicompartment neuron models (and the corresponding LFP) does not interact with other multicompartment neurons or the activity in the point-neuron network model, that is, there are no ephaptic interactions.

The first version of the hybrid scheme implemented in hybridLFPy (<https://INM-6.github.com/hybridLFPy>) is developed for random networks such as the layered cortical microcircuit model of Potjans and Diesmann (2014) that is our reference network. In contrast to this reference model that contains no spatial information, the upscaled models described in Section 2.1 assign spatial coordinates to the neurons within each layer but ignore information about cortical depth, and draw connections between neurons with probabilities depending on lateral distance. Modifications to the hybrid scheme to account for upscaled networks thus include:

- We use the lateral locations of the point neurons also for the multicompartment neuron models, and assign population-dependent somatic depths as in Hagen et al. (2016).
- We record the spiking activity from all neurons in the point-neuron network and associate each spike train to the corresponding neuron ID.
- Presynaptic neuron IDs are drawn for each multicompartment neuron using the same distance-dependent probability rule as is used when constructing the point-neuron network (the connectivity is thus statistically reproduced). The same distance-dependent delay rule is also implemented in the hybrid scheme, and can be set separately for each pair of populations.
- We compute the extracellular potential at 100 contact sites arranged on a square regular grid with each contact separated by $400\ \mu\text{m}$, similar to the layout of the Blackrock ‘Utah’ multi-electrode array. The local field potential is computed at the center of layer 2/3 (L2/3).
- LFPy, which implements the above forward model and is used internally in the hybrid scheme, accounts for periodic boundary conditions.

2.2.2 Modifications to LFPy to account for periodic boundary conditions

As the upscaling procedure of the 1mm^2 reference point-neuron network model incorporates periodic boundary conditions, we modify the forward-model calculations in LFPy (<https://LFPy.readthedocs.io>, Lindén et al., 2014; Hagen et al., 2018) to also account for such boundaries. The basic premise for this modification is that transmembrane currents of a neuron positioned near the network layer boundary should result in a fluctuation of the extracellular potential also due to sources across the boundary. This is analogous to input from network connections across the

boundaries resulting from the distance-dependent connectivity rule. Thus, for a current source located in location $\mathbf{r}_{jn} = (x_{jn}, y_{jn}, z_{jn})$ the extracellular potential in location \mathbf{r} is computed as the sum

$$\phi(\mathbf{r}, t) = \sum_{p=-M}^M \sum_{q=-M}^M \phi_{pq}(\mathbf{r}, t), \quad (23)$$

where $\phi_{pq}(\mathbf{r}, t)$ corresponds to the extracellular potential with horizontally shifted source coordinates $(x_{jn} + pL, y_{jn} + qL, z_{jn})$, L the network layer side length and $M = 2$ a chosen integer setting the number of ‘mirror’ sources to either side.

2.3 Statistical analysis

As simulation output, we consider the spiking activity of the point-neuron networks (Section 2.1.1), and corresponding multi-unit activity (MUA), LFP (Section 2.2) and current-source density (CSD) estimates. We use simulated output data only after an initial time period of T_{trans} to avoid startup transients, and compute all measures for the whole time interval of the following simulation duration T_{sim} . Parameters are given in Tables 3, 4 and 5.

2.3.1 Temporal binning of spike trains

Spike times t_i^s of the point-neuron networks simulated using temporal resolution dt are assigned to bins with width Δt . Temporally binned spike trains are used to compute pairwise spike-train correlations and population-rate power spectral densities, and to illustrate population-averaged rate histograms. The bin width Δt is an integer multiple of the simulation resolution dt . The simulation duration T_{sim} is an integer multiple of the bin width such that the number of bins is $K = T/\Delta t$. Time bins have indices $k \in \{0, 1, \dots, K - 1\}$, spanning time points in $t \in [k\Delta t, (k + 1)\Delta t)$.

2.3.2 Spatiotemporal binning of spike trains

In order to compute the propagation speed of evoked activity in the network, we perform a spatiotemporal binning operation of spiking activity in the network. As introduced in Section 2.1.1, neuron positions (x_i, y_i) of the point-neuron network are randomly drawn with $\{x_i, y_i\} \in [-L/2, L/2)$. We subdivide the spatial domain of each layer into square bins of side length Δl such that the integer numbers of bins along the x - and y -axis are $L_{\{x,y\}} = L/\Delta l$. The bin indices are $l_{\{x,y\}} \in \{0, 1, \dots, L_{\{x,y\}} - 1\}$, spanning $\{x, y\} \in [l_{\{x,y\}}\Delta l - L/2, (l_{\{x,y\}} + 1)\Delta l - L/2)$. Temporal bins of width Δt are defined as above. We compute for each population a spatially and temporally binned instantaneous spike-count rate in units of s^{-1} as the number of spike events from all neurons inside the spatial bin divided by Δt .

2.3.3 Current-source density (CSD) analysis

We estimate the current-source density (CSD) using the kernel CSD (kCSD) method introduced by Potworowski et al. 2012. The CSD is an estimate of the volume density of transmembrane currents nearby each LFP measurement site (in units of current per volume). Based on the Poisson equation in electrostatics,

$$\nabla(\sigma\nabla)\phi = -C, \quad (24)$$

which relates the electric potential $\phi \equiv \phi(\mathbf{r})$, conductivity $\sigma_e \equiv \sigma_e(\mathbf{r})$ (which is here assumed to be scalar as above), and current density $C \equiv C(\mathbf{r})$, one can make the assumption that the measured LFP at each electrode results from a sum of M current sources distributed across space. Similar to Łęski et al. 2011; Potworowski et al. 2012, we consider the underlying CSD as a product

$$\tilde{f}(x, y, z) = \tilde{f}(x, y)H(z), \quad (25)$$

where the term $\tilde{f}(x, y)$ describes a spatial profile in the horizontal xy -plane and $H(z)$ the step function along the vertical z -axis,

$$H(z) = \begin{cases} 1 & -h \leq z \leq h, \\ 0 & \text{otherwise.} \end{cases} \quad (26)$$

The variable h denotes the half-thickness of the current-generating region. Under the assumption of a linear (frequency-independent) and homogeneous (equal in all locations) conductivity, it follows that the electric potential in a location $(x, y, 0)$ is

$$f(x, y, 0) = \frac{1}{2\pi\sigma} \int \operatorname{arcsinh}\left(\frac{2h}{\sqrt{(x-x')^2 + (y-y')^2}}\right) \tilde{f}(x', y') dy' dx'. \quad (27)$$

We here choose to define $\tilde{f}(x, y)$ in terms of 2D Gaussians of the form

$$\tilde{b}_i(x, y) = \exp\left(-\frac{(x - x_i)^2 + (y - y_i)^2}{2\sigma_R^2}\right), \quad (28)$$

resulting in

$$b_i(x, y) = \frac{1}{2\pi\sigma_e} \int \operatorname{arcsinh}\left(\frac{2h}{\sqrt{(x - x')^2 + (y - y')^2}}\right) \tilde{b}_i(x, y) dy' dx'. \quad (29)$$

Introducing

$$\phi(x, y) = \mathcal{A}C(x, y) = \sum_{j=1}^M a_j b_j(x, y), \quad (30)$$

where $\mathcal{A} : \tilde{\mathcal{F}} \rightarrow \mathcal{F}$ is a linear operator connecting electric potentials and the underlying sources, the CSD is estimated as

$$C^*(x, y) = \tilde{\mathbf{K}}^T(x, y) \cdot \mathbf{K}^{-1} \cdot \mathbf{V}, \quad (31)$$

which minimizes the norm $\|\phi\|^2 = \sum_{i=1}^M |a_i|^2$. Here $\mathbf{V} = [\phi_1, \phi_2, \dots, \phi_N]^T$ is the observed LFP across channels, $\tilde{\mathbf{K}}^T(x, y) = [\tilde{K}_1(x_1, y_1, x, y), \tilde{K}_2(x_2, y_2, x, y), \dots, \tilde{K}_N(x_N, y_N, x, y)]$ and

$$\mathbf{K} = \begin{bmatrix} K(x_1, y_1, x_1, y_1) & \cdots & K(x_1, y_1, x_N, y_N) \\ \vdots & \ddots & \vdots \\ K(x_N, y_N, x_1, y_1) & \cdots & K(x_N, y_N, x_N, y_N) \end{bmatrix}, \quad (32)$$

defined in terms of the kernel functions $K(x, y, x', y') = \sum_{i=1}^M b_i(x, y) b_i(x', y')$ and cross-kernel functions $\tilde{K}(x, y, x', y') = \sum_{i=1}^M b_i(x, y) \tilde{b}_i(x', y')$. See Potworowski et al. 2012 for details on the procedure. We use the implementation of the 2D kCSD method available in Elephant (Electrophysiology Analysis Toolkit, <https://github.com/neuralensemble/elephant>), with default parameters $\sigma_e = 0.3 \text{ S/m}$, $M = 1000$, $h = 1 \text{ mm}$, $\sigma_R^2 = 0.23 \text{ mm}^2$, and return the estimate at the space spanned by the LFP electrodes with resolution 0.4 mm.

2.3.4 Calculation of MUA signal

For each electrode contact point located in L2/3, we compute a signal representative of the so-called multi-unit activity (MUA) signal that can be obtained from recordings of extracellular potentials by high-pass filtering the signal ($\gtrsim 500 \text{ Hz}$), followed by signal rectification, temporal smoothing, and downsampling (see, for example, Einevoll et al., 2007). In a biophysical modeling study (Pettersen et al., 2008) it is shown that this signal is approximately linearly related to the firing rate of the local population of neurons in the vicinity of the measurement device. Neuron coordinates (x_i, y_i) of the upscaled point-neuron network are randomly drawn on the interval $\{x_i, y_i\} \in [-L/2, L/2]$. We subdivide the layers into square bins of side length $\Delta l_{\text{MUA}} = 0.4 \text{ mm}$ resulting in 10 bins along the x - and y -axis, respectively. Each electrode contact point is located at the center of the respective bin. We also define temporal bins of width Δt . We then compute for each population a spatially and temporally binned spike-count rate in units of s^{-1} by summing the number of spike events from all neurons inside the spatial bin and divide by the width of the temporal bin Δt . We then define the MUA signal as the sum of the per-bin contributions of the populations L2/3E and L2/3I.

2.3.5 Visual analysis

The *spike raster* diagrams or dot displays show information on spiking activity. Each dot marks a spike event, and the dot position along the horizontal axis denotes the time of the event. Spike data of different neuron populations are stacked and the number of neurons shown is proportional to the population size. Within each population, neurons are sorted according to their lateral x -position and arranged accordingly on the vertical axis of the dot display.

We compute *population-averaged rate histograms* by deriving the per-neuron spike rates in time bins Δt and units of s^{-1} , averaged over all neurons per population within the center disc of 1 mm^2 . The corresponding histogram shows the rates in a time interval of $\pm 25 \text{ ms}$ around the occurrence of a thalamic pulse. Such a display is comparable to the Peri-Stimulus Time Histogram (PSTH, Perkel et al., 1967) that typically shows the spike count summed over different neurons or trials versus binned time.

Image plots with color bars can have a linear or a logarithmic scaling as specified in the respective captions. Since values of the distance-dependent cross-correlation functions can be positive or negative, we plot these with linear scaling up to a threshold, beyond which the scaling is logarithmic.

2.3.6 Statistical measures

Per-neuron spike rates ν are defined as the number of spikes per neuron during each simulation divided by the simulation duration T_{sim} . Distributions of per-neuron spike rates are computed from all spike trains of each population separately for an interval from 0 to 30 s^{-1} using bins of width 1 s^{-1} . Histograms are normalized such that the cumulative sum over the histogram equals unity. We define the mean rate per population $\bar{\nu}$ as the arithmetic mean of all per-neuron spike rates of each population.

The *coefficient of local variation* LV is a measure of spike-train irregularity computed from a sequence of length n of consecutive inter-spike intervals T_i (Shinomoto et al., 2003, Equation 2.2), defined as

$$LV = \frac{1}{n-1} \sum_{i=1}^{n-1} \frac{3(T_i - T_{i+1})^2}{T_i + T_{i+1}}. \quad (33)$$

Like the conventional coefficient of variation CV (Shinomoto et al., 2003, Equation 2.1), a sequence of intervals generated by a stationary Poisson process results in a value of unity, but the LV statistic is less affected by rate fluctuations compared to the CV ; thus, a non-stationary Poisson process should result in $LV \approx 1$. We compute the LV from the inter-spike intervals of the spike trains of all neurons within each population. Distributions of LV s are computed using bins of width 0.1, and histograms are normalized such that the cumulative sum over the histogram equals unity. We define the mean LV per population \overline{LV} as the arithmetic mean of all LV s of each population.

The *Pearson (product-moment) correlation coefficient* CC is a measure of synchrony that is defined for two signals u and v as

$$CC_{uv} = \frac{\text{cov}(u, v)}{\sqrt{\text{cov}(u, u) \text{cov}(v, v)}}, \quad (34)$$

with the covariance denoted by cov . The calculation is implemented using `numpy.corrcoef`. To compute distributions of correlation coefficients from spike trains, we randomly select 1000 neurons per population and assign their spike times to temporal bins with width $\Delta t_{CC} = 5 \text{ ms}$ (see Section 2.3.1). Then, we compute pairwise CC s for the spike counts $u = n_i$ and $v = n_j$ of selected neurons i from a population X and neurons j from a population Y (ignoring autocorrelations). Within each population, meaning $X = Y$, the CC is denoted by $E - E$ for an excitatory population or $I - I$ for an inhibitory population. Correlations between neurons from the excitatory and the inhibitory population in each layer are denoted by $E - I$. CC histograms have bins of width 0.003, are restricted to a range with a minimum and maximum CC of ± 0.08 , respectively, and are normalized such that the integral over the histogram equals unity. We also compute correlation coefficients for assessing the distance dependency of spikes, LFP, CSD, and MUA signals. In these cases, u and v are LFP, CSD, or MUA time series in different spatial locations. For spikes, we sample 40 excitatory and 10 inhibitory spike trains, bin them as above, compute their correlation coefficients (ignoring autocorrelations), and plot them according to distance between the pairs of neurons.

Coherences are computed as

$$\gamma_{uv}(f) = \frac{|S_{uv}(f)|}{\sqrt{S_{uu}(f)S_{vv}(f)}}, \quad (35)$$

where $S_{uv}(f)$ is the cross-spectral density between u and v , and $S_{uu}(f)$ and $S_{vv}(f)$ are the power spectral densities (PSDs) of each signal. The *cross-spectral density* and *power spectra* are computed using Welch's average periodogram method (Welch, 1967) as implemented by `matplotlib.mlab`'s `csd` and `psd` functions, respectively, with number of data points used in each block for the fast Fourier transform (FFT), that is, segment length $N_{\text{FFT}} = 256$, overlap between segments $N_{\text{overlap}} = 192$ and signal sampling frequency $F_s = 2 \text{ kHz}$. To compute the *population-rate power spectral density*, we use the spike trains of all neurons per population (in Figure 3N and H only within the center disc of 1 mm^2), resampled into bins of size Δt , and with the arithmetic mean of the binned spike trains subtracted.

The effect of thalamic pulses is analyzed by means of *distance-dependent cross-correlation functions* $CC^\nu(\tau, r)$ evaluated for time lags τ . We discretize the network of size $L \times L$ into an even number of square bins of side length Δl . The spike trains from all neurons within each spatial bin are resampled into time bins of size Δt and averaged across neurons to obtain spatially and temporally resolved per-neuron spike rates. We select spatial bins on the diagonals of the network such that each distance to the center with coordinates $(0, 0)$ is represented by four bins. For 14 distances from consecutive spatial bins along the diagonal, we compute the temporal correlation function between the rates in the respective spatial bins with a binary vector containing ones at spike times of the thalamic pulses and zeros elsewhere, and then average over the four spatial bins at equal distance. The sequences are normalized by subtracting their mean and dividing by their standard deviation. Correlations between the sequences u and v with time steps k and the length of the sequences K are then computed as

$$CC_{u,v}(\tau) = \frac{1}{K} \sum_{k=1}^K u_{k+\tau} v_k \quad (36)$$

for $\tau \in [-25, 25]$ ms in steps of Δt . Finally, we subtract the baseline correlation value, obtained by averaging over all negative time lags (before thalamic activation at $\tau = 0$), and get $CC^\nu(\tau, r)$.

To estimate the *propagation speed* v_{prop} from the cross-correlation functions, we find for each distance the time lag corresponding to the largest CC^ν . Values of CC^ν smaller than 10% of the maximum of all CC^ν per population across distances and time lags are excluded. We further exclude distances smaller than the thalamic radius $R_{\text{TC}}^{\text{pulse}}$ plus the spatial width of thalamic connections σ_{TC} because a large part of neurons within this radius are simultaneously receiving spikes directly from thalamus upon thalamic pulses. A linear fit for the distance as function of time lag, $r_p(\tau) = r_{p,0} + v_p \cdot \tau$, yields the speed v_p and its fitting error, the standard deviation $\sigma_{v,p}$. We compute the speed for different populations p and obtain the propagation speed as weighted mean with its uncertainty:

$$v_{\text{prop}} = \frac{\sum_p v_p / \sigma_{v,p}^2}{\sum_p 1 / \sigma_{v,p}^2}, \quad \sigma_{v,\text{prop}} = \sqrt{\frac{1}{\sum_p 1 / \sigma_{v,p}^2}}. \quad (37)$$

2.3.7 Curve fitting

For certain measures, such as pairwise correlation coefficients computed for different distances between LFP electrode locations, we fit exponential functions of the form

$$y(r) = a \cdot e^{-r/b} + c, \quad (38)$$

where $\beta = (a, b, c)$ are constant parameters that minimize the sum $\sum_{i=1}^m |y_i(r_i) - y(r_i, \beta)|^2$ for the m data points y_i computed for distance r_i . The parameter fitting is implemented using the non-linear least squares function `curve_fit` provided by the `scipy.optimize` module, with initial guess $\beta = (0.1, 0.1, 0.1)$. Goodness of fit is quantified by the coefficient of determination, defined as

$$R^2 = 1 - \frac{\sum_{i=1}^m (y_i(r_i) - y(r_i, \beta))^2}{\sum_{i=1}^m (y_i(r_i) - \bar{y})^2}, \quad (39)$$

where \bar{y} is the mean of the observed data.

2.4 Software accessibility

We here summarize the details of software and hardware used to generate the results presented throughout this study. Point-neuron network simulations are implemented using the SLI interface of NEST v2.12.0 (Kunkel et al., 2017), and Python v2.7.11. We use the same network implementation for reference and all upscaled models and switch between them by adjusting parameters. Parameter scans rely on the parameters module of NeuroTools (<http://neuralensemble.org/NeuroTools/>). LFP signals are computed using NEURON v7.5 and LFPy from <http://lfp.pygithub.io/> (branch 'som_as_point_periodic' at SHA:4cab667), hybridLFPy (<https://github.com/INM-6/hybridLFPy>, branch 'LFPy_dev' at SHA:0f1bfb2). Analysis and plotting rely on Python with numpy v1.10.4, SciPy v0.17.0, and matplotlib v2.1.2. All simulations and analyses are conducted on the JURECA supercomputer (http://www.fz-juelich.de/ias/jsc/EN/Expertise/Supercomputers/JURECA/JURECA_node.html) based on Intel Xeon E5-2680 v3 Haswell CPUs running the CentOS 7 Linux distribution. Simulations are run using 1152 and 2304 physical cores for the network and LFP simulations, respectively. All source codes to reproduce these results and figures will be made publicly available upon final publication of this manuscript.

3 Results

3.1 Upscaling of a cortical microcircuit model using lateral distance-dependent connectivity

Starting with a model of the cortical microcircuit (the reference model, see Potjans and Diesmann, 2014), we construct full-scale multi-layer neuronal network models with distance-dependent connectivity via the upscaling procedure described in Section 2.1.2. The full network descriptions are provided in Section 2.1.1 and in Tables 1 and 2. Here, we point out similarities and differences between the reference model and an upscaled model with parameters set to the values given in Tables 3-5. We refer to this parameterization as the 'base parameters'. Figure 1A illustrates the reference model next to the laterally upscaled version. The reference model comprises almost 80,000 neurons under 1 mm^2 of cortical surface area, while the upscaled model consists of approximately 1.2 million neurons and covers an area of $4 \times 4 \text{ mm}^2$, similar to the area covered by the Utah multi-electrode array. To illustrate their connectivities, the figure shows in both network sketches incoming connections from population L5E to an example target neuron in population L4E. In the reference model without spatial structure, source neurons are picked randomly from the source population. In the upscaled model, source neurons are picked around the target neuron in layer 4 according

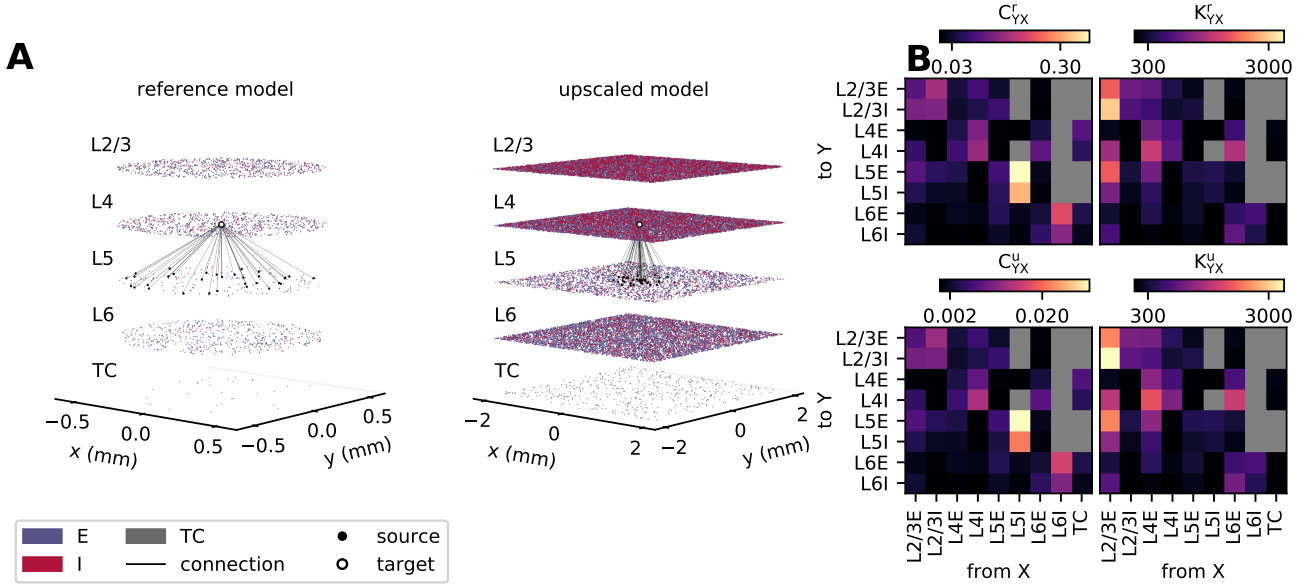


Figure 1: Layered cortical point-neuron network models. **A** Illustrations of the network geometry of the reference model (left, 1 mm^2 cortical microcircuit, introduced by Potjans and Diesmann, 2014) and an upscaled model (right, $4 \times 4 \text{ mm}^2$ cortical layers). Both models consist of four cortical layers (L2/3, L4, L5, L6) with an excitatory (E) and an inhibitory (I) population each, and an external thalamic population (TC). Colored dots represent individual neurons at their (x, y) -coordinates; excitatory neurons in blue, inhibitory neurons in red, and thalamic neurons in gray. The number of neurons shown per population is reduced by a factor 32 compared to the actual neuron number in each network to not saturate the illustrated layers. Black lines illustrate convergent connections from sources in L5E (black dots) to a target neuron in L4E (white dot). In-degrees correspond to the actual average in-degrees in both models rounded to the nearest integer: 33 in the reference model and 39 in the upscaled model. Sources are drawn at random in the reference model, but with lateral distance dependency (Gaussian-shaped profile) in the upscaled model. **B** Network connectivity of the reference model (top panels) and the upscaled model (bottom panels). Upscaled connection probabilities are computed as in Equation 4. Left panels show color-coded connection probabilities C_{YX}^r and C_{YX}^u (different color code) with the values given in Tables 4 and 5, and right panels show derived in-degrees K_{YX}^r and K_{YX}^u (same color code). Color maps have linear scaling with zero-values masked in gray.

to distance-dependent probabilities with Gaussian profiles of outgoing connections from layer 5 excitatory neurons. The width of the profile is 0.3 mm which is the average value σ_0 from the connectivity data underlying the reference model, see Equation 1. A major fraction of source neurons falls into the center 1 mm², justifying the assumption of random connectivity in the reference model.

The population-specific connection probabilities in the reference model C_{YX}^r , shown in Figure 1B, are equal to those in Potjans and Diesmann (2014, Table 5). The upscaling procedure yields connection probabilities C_{YX}^u that are decreased by approximately one order of magnitude in comparison to the reference model. The derived in-degrees K_{YX}^u , however, are slightly larger than K_{YX}^r for all population pairs. This is expected since the upscaling procedure adds connections at distances not accounted for within the limited extent of the reference model.

For the final upscaled model, we increase the excitatory and decrease the inhibitory spatial widths of the connection probability profiles (Equation 12) compared to the average value σ_0 of the reference model to $\sigma_E = 0.35$ mm and $\sigma_I = 0.1$ mm, respectively. Accumulating experimental data indicate Gaussian or exponentially decaying connection probabilities with distance for both excitatory and inhibitory local connections; see, for example, the review by Boucsein et al. (2011), or Hellwig (2000) for pyramidal cells in layers 2 and 3 of rat visual cortex, Budd and Kisvárdy (2001) for clutch cells in layer 4 of cat visual cortex, Perin et al. (2011) for pyramidal cells in layer 5 of rat somatosensory cortex, Levy and Reyes (2012) for pyramidal cells and (non-)fast-spiking inhibitory cells in deep layer 2/3 and layer 4 of mouse auditory cortex, Schnepel et al. (2015) for excitatory input to pyramidal neurons in layer 5B of rat somatosensory cortex, Jiang et al. (2015) for pyramidal cells and different interneurons in layers 1, 2/3, and 5 of mouse visual cortex, Packer and Yuste (2011) for parvalbumin-positive cells connected to pyramidal cells in multiple layers of mouse neocortex, and Reimann et al. (2017) for morphologically classified cell types in an anatomical reconstruction and simulation of a rat hindlimb somatosensory cortex column (Markram et al., 2015). Such profiles result largely from the axo-dendritic overlap of the neuronal morphologies (Amirikian, 2005; Brown and Hestrin, 2009; Hill et al., 2012). Broader excitation than inhibition is in line with the experimental data since excitatory neurons, in particular pyramidal types, develop axons with larger horizontal reach compared to most inhibitory interneuron types (Budd and Kisvárdy, 2001; Binzegger et al., 2004; Buzás et al., 2006; Binzegger et al., 2007; Stepanyants et al., 2008, 2009; Ohana et al., 2012). Certain interneuron types may, however, have elaborate axons that span and form synapses across different layers within the cortical column (see, for example, Markram et al., 2015, Figure 2). Others may also form longer-range lateral connections (McDonald and Burkhalter, 1993).

The chosen value for the conduction speed $v = 0.3$ mm/ms is in the range of speeds reported for action potential propagation along unmyelinated nerve fibers in cortex. Conduction speeds can be measured, for example, in brain slices using electrical stimulation combined with electrophysiological recordings: 0.2 – 0.35 mm/ms in guinea pig hippocampus (Andersen et al., 1978), $1 / (3.5 \text{ ms/mm}) \approx 0.29$ mm/ms at 34 – 35°C in cat visual cortex (Hirsch and Gilbert, 1991), 0.3 mm/ms at 35°C in rat hippocampus (Berg-Johnsen and Langmoen, 1992), 0.15 – 0.55 mm/ms at $31 \pm 0.5^\circ\text{C}$ in rat visual cortex (Murakoshi et al., 1993), 0.28 – 0.48 mm/ms (mean \pm standard deviation, 0.37 ± 0.37 mm/ms) at 35°C in cat motor cortex (Kang et al., 1994), 0.28 ± 0.19 mm/ms at 34°C in rat visual cortex (Lohmann and Rörig, 1994), 0.06 – 0.2 mm/ms at 34 – 35°C in rat somatosensory cortex (Salin and Prince, 1996), 0.508 mm/ms at 32 – 35°C in rat somatosensory cortex (Larkum et al., 2001, back-propagating action-potentials in dendrites), and 0.34 – 0.44 mm/ms at $34 \pm 1^\circ\text{C}$ in rat somatosensory cortex. Some of these values are likely underestimated because the separation of conduction speed from both the synaptic delay and spike initiation time is difficult (Hirsch and Gilbert, 1991). The bath temperature is provided if specified by the study because the conduction speed and the timing of synaptic processing depend strongly on environmental temperature (Katz and Miledi, 1965; Berg-Johnsen and Langmoen, 1992; Sabatini and Regehr, 1996; Hardingham and Larkman, 1998). We are here primarily interested in physiologically relevant body temperatures. Connections in the upscaled models have a delay offset $d_0 = 0.5$ ms comparable to the experimental estimates 0.5 – 1 ms (Murakoshi et al., 1993), 0.6 – 0.8 ms (Hirsch and Gilbert, 1991) and 0.6 ms (Kang et al., 1994). To account for this variability in experimental data the delays have an additive normally distributed random component, see Equation 18. From a theoretical perspective, a wide delay distribution expands the region of stability in the phase space of stationary network activity (Brunel, 2000, Section 5.2).

Although delay offset and conduction speed have the same parameter values for excitatory and inhibitory connections in the upscaled model, the effective delays (Equation 10) within a given surface area differ due to the different space constants of the connectivity. Computing the mean delay for connections within a circle of 1 mm² with the respective spatial widths according to Equation 10 results in a shorter mean delay for inhibitory connections. The effective excitatory and inhibitory delays up to single decimal precision are 1.6 ms and 0.9 ms, respectively. Hence, a shorter inhibitory delay in a network model without distance dependence like the reference model is justified by a narrower inhibitory connectivity of the corresponding model with spatial structure.

The spike raster in Figure 2A shows that the reference model produces asynchronous irregular spiking with low firing rates (Softky and Koch, 1993; Brunel and Hakim, 1999; Brunel, 2000) across all populations. Network oscillations appear as weakly pronounced vertical stripes. The firing rates are on average higher for inhibitory populations

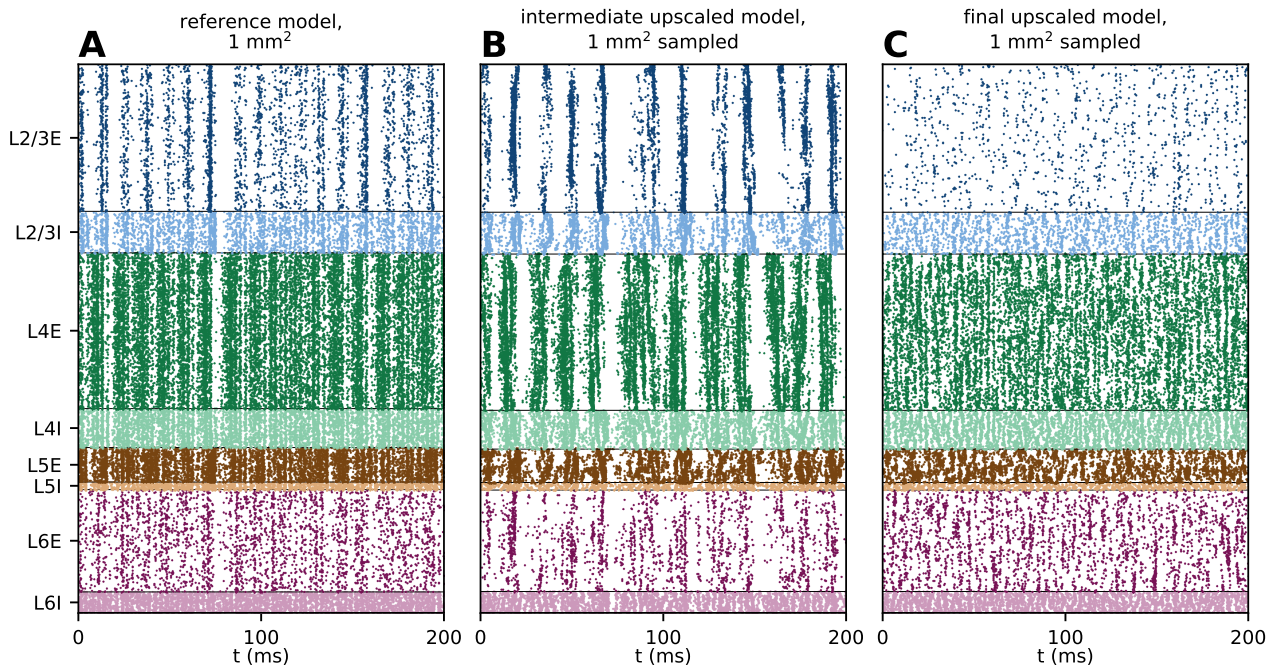
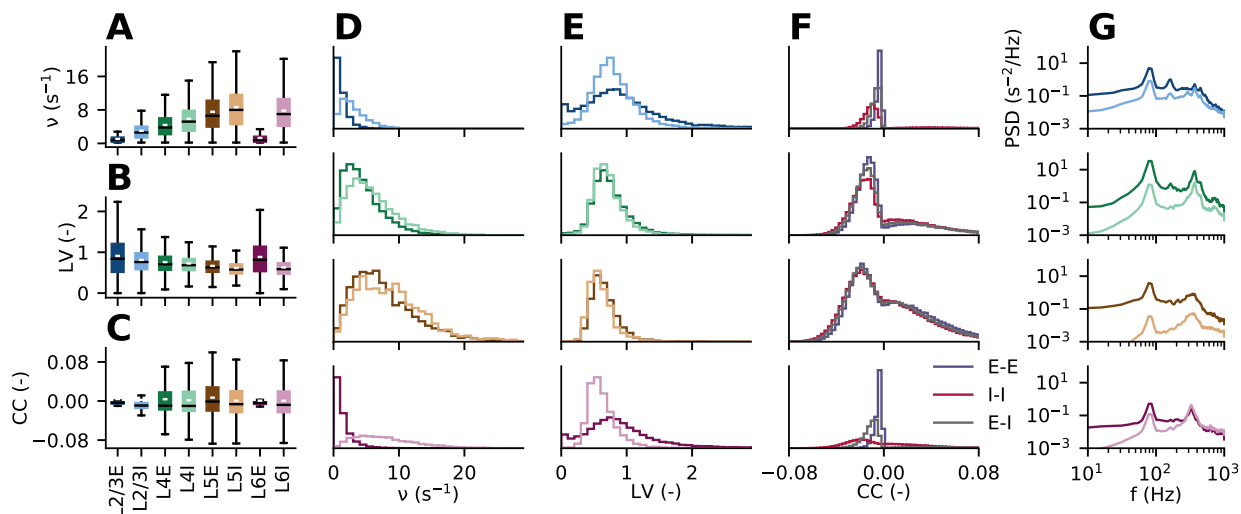
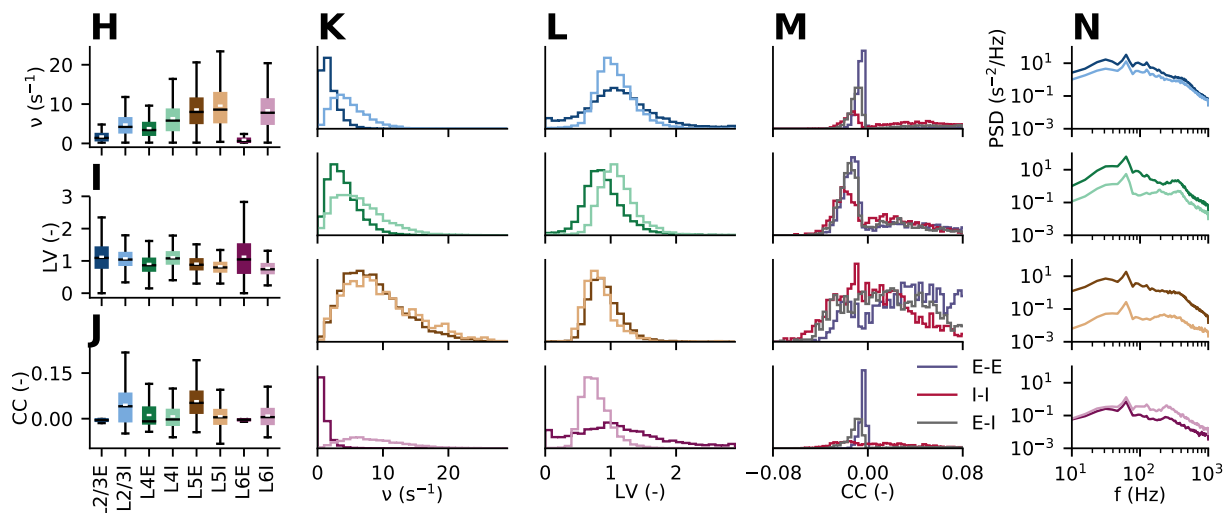


Figure 2: **Spiking activity of the reference, intermediate upscaled, and final upscaled models.** **A** Spike raster showing the spike times (horizontal) of all neurons of the reference model network (microcircuit below 1 mm^2 of cortical surface, no spatial connectivity structure) vertically organized according to layer (axes labeling and colors) and neuron type (lighter for inhibitory). **B** Spike raster of a model network upscaled to $4 \times 4 \text{ mm}^2$ with distance-dependent connectivity. The intermediate connection probabilities C_{YX}^{int} resulting from the upscaling procedure are not modified ($\delta C_{YX} = 0$). Spike times of all neurons located inside a disc of 1 mm^2 shown (neurons are always sorted vertically according to their x -position). **C** Same as panel B, but with modified connection probabilities C_{YX}^{u} according to δC_{YX} given in Table 5. The parameters of the final upscaled model are referred to as 'base parameters' and given in Table 5.

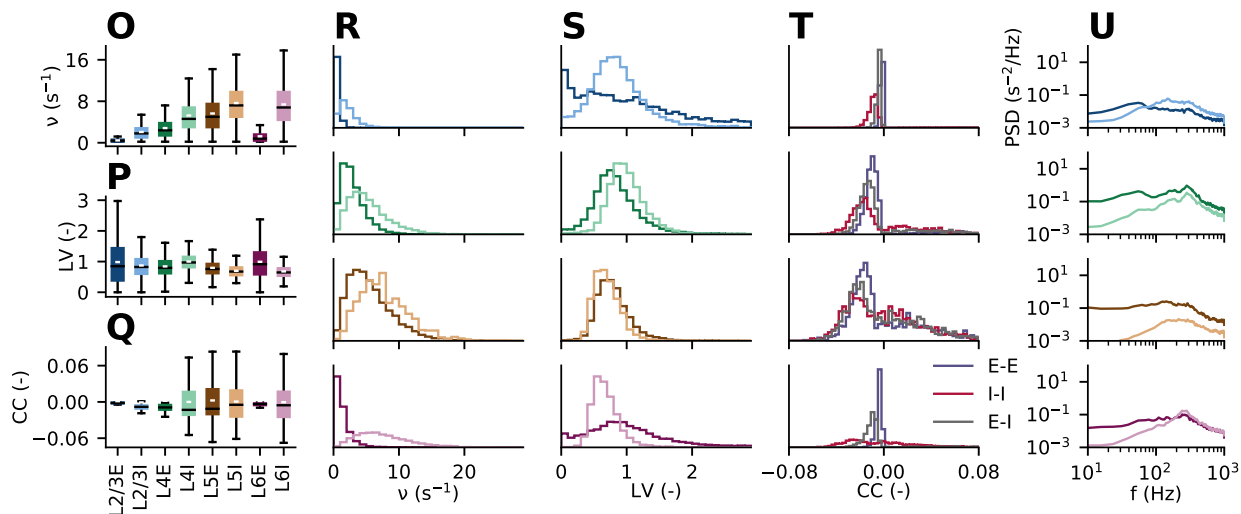
reference model, 1 mm²



intermediate upscaled model, 1 mm² sampled



final upscaled model, 1 mm² sampled



than for excitatory populations within the same layer, see Figure 3A, and the mean illustrated in each box-chart is larger than the median. The latter corresponds to the long-tailed distributions of spike rates in Figure 3D with most neurons firing at lower rates, while few neurons have high ($> 20\text{s}^{-1}$) rates. This type of non-symmetric distribution of firing rates in the model resembles approximately lognormally distributed firing rates observed experimentally (reviewed in Buzsáki and Mizuseki, 2014). The mean values of the coefficients of local variation (Figure 3B,E) are slightly below unity, indicating more regular spike trains than events produced by a Poisson point process ($LV = 1$). The distributions are broad, that is, a fraction of neurons in each population has spike-train statistics with $LV > 1$. The mean LV values are comparable to values observed in visual cortex across different species (Mochizuki et al., 2016, Figure 5B). The box charts in Figure 3A,B are similar to (Potjans and Diesmann, 2014, Figure 6) showing firing rates and the conventional coefficient of variation (Shinomoto et al., 2003, Equation 2.1). The Pearson correlation coefficients (Figure 3C,F) are distributed and have a mean close to zero. Weak pairwise spike-train correlations (with mean values < 0.1 using 50ms windows) are reported, for example, by Ecker et al. (2010) who record from nearby neurons in primary visual cortex of awake monkey under different stimulation conditions, and by Renart et al. (2010) in somatosensory and auditory cortex of anesthetized rats. The latter study finds that the mean correlations are not distance-dependent, but their standard deviations decay with distance (their Figure S11). The authors also include a theoretical analysis of this phenomenon for networks of infinite size and find that excitatory and inhibitory synaptic currents are anticorrelated, thereby leading to a suppression of shared-input correlations, and, hence, weak overall correlations in the asynchronous state. Tetzlaff et al. (2012) and Helias et al. (2014) identify the mechanism underlying the suppression of shared-input correlations for the realistic case of finite-sized networks, which differs from the mechanism in the infinite-size limit. They show that the decorrelation is due to dominant negative feedback, which leads to small correlations in both excitatory-inhibitory and purely inhibitory networks.. However, depending on factors such as brain state and distance, stronger correlations are also detected in some cases (Smith and Kohn, 2008; Kriener et al., 2009; Peyrache et al., 2012; Smith et al., 2012; Doiron et al., 2016; Rosenbaum et al., 2017). The population-rate power spectral densities in Figure 3G show that the power tends to be higher in the activity of excitatory compared to inhibitory populations due to the overall larger density of excitatory neurons, except for layer 6, where the inhibitory rate is very high compared to the excitatory rate. Across layers the power is highest in layer 4, explained by the comparatively high spike rates and high cell densities. The power spectra reveal two dominant oscillation frequencies of the network in the low and high gamma ranges ($\sim 80\text{Hz}$ and $\sim 320\text{Hz}$). Recent theoretical work by Bos et al. (2016) provides insight into the main pathways between the recurrently connected populations involved in generating these high-frequency oscillations. The low-gamma peak is predominantly generated by a sub-circuit of layer 2/3 and layer 4 populations of excitatory and inhibitory neurons (pyramidal-interneuron gamma or “PING” mechanism (Leung, 1982; Börgers and Kopell, 2003, 2005), while the high-gamma peak results from interneuron-interneuron interactions (interneuron-interneuron gamma or “ING” mechanism, see Whittington et al., 1995; Wang and Buzsáki, 1996; Chow et al., 1998; Whittington et al., 2000) within each layer. See Buzsáki and Wang (2012) for a review on the various mechanisms underlying gamma oscillations.

Before we discuss the final upscaled model in comparison to the reference model, we first introduce an intermediate model in order to differentiate between effects of pure upscaling and effects of modified connection probabilities on network activity. This intermediate model is upscaled as described in Section 2.1.2 resulting in connection probabilities C_{YX}^{ui} derived directly from C_{YX}^{r} (from Equation 5). No connection probabilities are otherwise perturbed ($\delta C_{YX} = 0$ for all X and Y). All model parameters are as specified in Tables 3-5 apart from the connection probabilities and the in-degrees of external input, which are derived as specified in Section 2.1.2. This intermediate model covers an area of $4 \times 4\text{mm}^2$, but we here choose to analyze only the spiking activity of neurons inside a disc of 1mm^2 at the center to obtain a representative sample for comparison with the reference model in terms of neuron numbers and spatial scale. The spike raster of the intermediate model (Figure 2B) exhibits by visual inspection spatially inhomogeneous activity and network synchrony that are more pronounced than observed in the reference model. Compared to the reference model, spike-train correlations in this intermediate model are increased by approximately an order of magnitude (Figure 3J,M), the coefficients of local variation are slightly increased (Figure 3I), and finally the overall power in the rate spectra is increased across all frequencies (Figure 3N). The spectra also exhibit reduced

Figure 3 (preceding page):

Statistics of spiking activity of the reference, intermediate upscaled, and final upscaled models. A–G Statistics of spiking activity of reference model shown in Figure 2A. **A** Heterogeneity of spike rates ν for each population (horizontal black lines: median, short white lines: mean, boxes in population-specific colors: lower and upper quartiles of the data, whiskers extend to most extreme observations within $1.5 \times \text{IQR}$ beyond the IQR (interquartile range) without outliers, see documentation of `matplotlib.pyplot.boxplot`). **B** Coefficients of local variation LV , see Equation 33. **C** Pearson correlation coefficients CC , see Equation 34. **D** Distributions of spike rates ν . **E** Distributions of coefficients of local variation LV . **F** Distributions of Pearson correlation coefficients CC . **G** Population-rate power spectral densities PSD . **H–N** Same as panels A–G for spiking activity of intermediate model shown in Figure 2B. **O–U** Same as panels A–G for spiking activity of upscaled model shown in Figure 2C.

low- and high-gamma peaks, and the activity is generally more broadband.

The high global synchrony observed in the spiking of the intermediate upscaled model is most likely exaggerated. There is accumulating evidence that the typical operating regime of sensory cortices is asynchronous and irregular in particular when no particular stimulus is present. Measures of LFP signals, which are assumed to mainly reflect synaptic activity, in for example visual cortex also do not show pronounced peaks in their spectra in the absence of stimuli (see, for example, Berens et al., 2008; Jia et al., 2011; Ray and Maunsell, 2011; Jia et al., 2013a; van Kerkoerle et al., 2014). We therefore modify the network to suppress the amplitudes of the two dominant oscillations in the low- and high-gamma range, and reduce their frequencies to better resemble the low and high-gamma peaks more commonly reported in the literature. For the final upscaled model, we adapt connection probabilities by applying the modifications δC_{YX} given in Table 5. The connection probabilities in the reference model are estimated across different areas and species and are merely suggestive of typical cortical connectivity—we therefore consider small modifications to these values to be within the bounds of uncertainties of these probabilities. Our choices on which connections to perturb rely on the framework developed by Bos et al. (2016) who provide a ‘sensitivity measure’ that relates population rate spectra to the connectivity of the underlying neuron network in a systematic manner. With the example of our reference model, they expose which individual connections are crucial for peak amplitudes and frequencies of emerging oscillations, and demonstrate how modifications of these connections affect the power spectra. By applying this sensitivity measure to the intermediate upscaled network, we find that its rate spectra are primarily shaped by the same specific connections as in the reference network. To stabilize the circuit, Bos et al. (2016) reduce the number of connections from L4I to L4E of the reference model for their analysis. With the same aim, we here reduce the connection probability from L4I to L4E and also increase that from L4I to L4I. Both of these modifications reduce amplitude and frequency of the low-gamma peak (Bos et al., 2016, Figure 8A for L4I-L4I). In addition, we increase the number of connections slightly from L5I to L5E and reduce the number of connections from L5I to L5I to further decrease the amplitude of this peak. A decrease of the number of connections from L5E to L5I amplifies low-frequency oscillations (Bos et al., 2016, Figure 8B). The resulting spike raster of the final upscaled model, similarly sampled in the center 1 mm^2 , exhibits temporally and spatially more homogeneous activity (Figure 2C) compared to the reference and intermediate networks. The mean spike-train correlations (Figure 3Q) are even lower than in the reference model. The power spectra have overall reduced power and its peaks are attenuated (Figure 3U). Most visible in populations L2/3E and L4E, a broad low-gamma peak spans roughly 40–60 Hz. Across all interneuron populations, a broad high-gamma peak above 100 Hz is present. The per-population spike rates of the reference model are now largely retained in the upscaled model (Figure 3O), as the upscaling procedure preserves the mean input of the neurons (see Section 2.1.2). The coefficients of local variation (Figure 3P) are similar to those of the reference model, although the LV of L4I is increased, which we also observe in the intermediate model (Figure 3H).

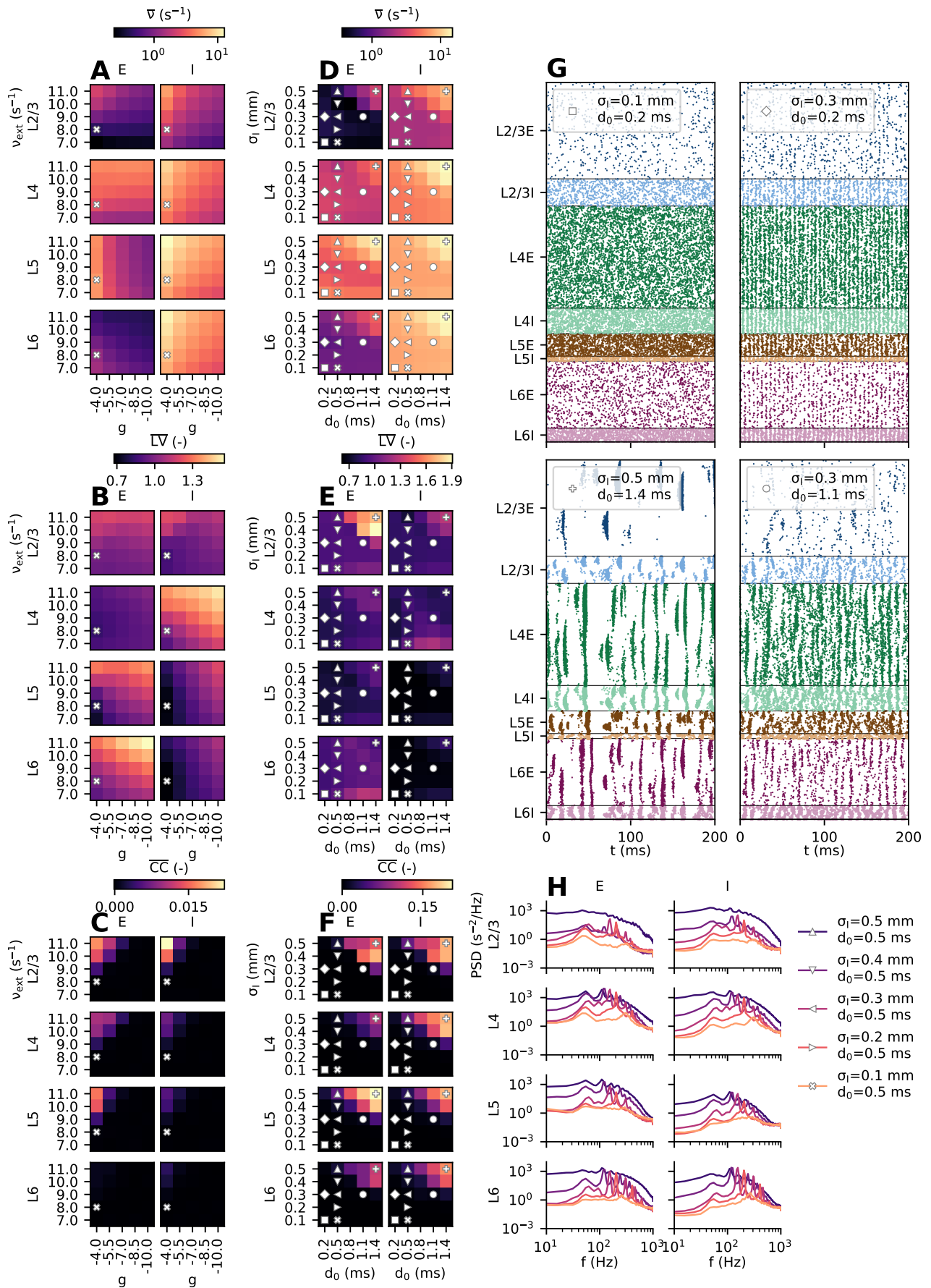
3.2 Spiking activity of the point-neuron networks

We have so far established an upscaling procedure of the reference network from an area of 1 mm^2 to an area of 16 mm^2 , which includes small perturbations to connection probabilities between key pre- and post-synaptic populations. The final upscaled network exhibits a stable network state that (1) is asynchronous and irregular across populations, (2) preserves the population rates, (3) preserves the distribution of firing rates, (4) preserves the variability of spike trains, (5) has very low average pairwise spike-train correlations, and (6) has rate spectra without pronounced peaks. We next investigate the spontaneous behavior around this network parameterization (‘base parameters’) by varying external input rates, inhibitory feedback weights, spatial connection widths, and the delay offset, which are all hard to constrain with available experimental data. We also study evoked thalamocortical activity in different network states in order to quantify the lateral propagation speed of the evoked network response, motivated by reports of propagating cortical activity.

3.2.1 Sensitivity to parameter perturbation during spontaneous activity

We here explore the state space of the upscaled network model by running parameter scans of both global network parameters (external input rate and inhibitory weights) and parameters governing distance-dependent connectivity (width of inhibition and delay offset). Theoretical work exposes a crucial sensitivity to network parameters studying the existence and stability of diverse dynamical states (Brunel, 2000; Roxin et al., 2005; Senk et al., 2018). However, experimental data from the literature are often sparse and disparate and the mapping of measured quantities to specific model parameters is not straightforward. Therefore, an exploration of the parameter space is necessary in order to characterize the range of possible model behaviors given the experimental constraints on the parameter values and also to obtain an intuition of the model behavior.

We first choose to vary the rate of the external Poisson input ν_{ext} and the relative inhibitory weight g . As shown in a simpler, analytically tractable case (Brunel, 2000), spatially unstructured networks of randomly and sparsely



connected excitatory and inhibitory leaky integrate-and-fire neurons can transition between distinct activity states with respect to the regularity of individual neuron firing and the synchrony of population activity upon changing these two parameters. Jumps in \bar{LV} (or the conventional coefficient of variation CV , see Shinomoto et al. 2003, Equation 2.1) and \overline{CC} during parameter scans of comparable two-population networks typically indicate transitions between states. It is, however, not a priori clear whether or not this analytical insight obtained with a smaller random network generalizes to spatially extended networks incorporating multiple layers and realistic density of neurons and connections such as our upscaled network model. Mehring et al. (2003, Figure 2), Voges and Perrinet (2010, Figure 4) and Voges and Perrinet (2012, Figure 2) study the same parameter space with spatially organized network models; however, only in single-layer and diluted networks.

While the mean population rates $\bar{\nu}$ in a two-population network typically increase when increasing ν_{ext} or decreasing g (see Mehring et al. (2003, Figure 2D), Voges and Perrinet (2010, Figure 4) and Voges and Perrinet (2012, Figure 2) for examples), Figure 4A shows that a similar trend does not appear for all populations of our multi-layer upscaled model. Within the parameter range tested, the mean rate of L4E is nearly unaffected upon varying g , and varying ν_{ext} has little effect on the rate of L5E. For L6E, the trend is even reversed. Different responses in different populations is explained by the population-specific network connectivity and competing inhibition and excitation between the different populations. Both recurrent (excitatory and inhibitory) and external (only excitatory) in-degrees and corresponding presynaptic rates result in population-specific means and variances of synaptic inputs. Spike-train irregularity, here quantified by the mean coefficient of local variation \overline{LV} in Figure 4B, also shows different trends per population. For all populations, the \overline{LV} increases when increasing ν_{ext} . Increasing g results in an increased \overline{LV} only in layers 4 to 6, while the effect on L2/3 does not show a clear dependency on either parameter in the tested parameter range. The \overline{LV} remains below 1 across the whole parameter space for populations L4E and L6I, while the highest values (above 1.3) are observed in L4I and L6E. Mean pairwise spike train correlations \overline{CC} in Figure 4C, increase for all populations by increasing ν_{ext} and decreasing g .

Next, we vary the spatial width σ_I of inhibitory connections and the delay offset d_0 , to assess the sensitivity of the upscaled network dynamics to variations in their chosen values. Although inhibitory spatial widths in terms of lateral axonal branching patterns are generally assumed to be shorter than excitatory widths (Stepanyants et al., 2009), estimates for the local excitatory and inhibitory decay of connection probabilities are broadly distributed and differ between brain areas, pre- and post-synaptic neuron types, and species (Hellwig, 2000; Budd and Kisvárdy, 2001; Boucsein et al., 2011; Kätzel et al., 2011; Perin et al., 2011; Hill et al., 2012; Levy and Reyes, 2012; Jiang et al., 2015; Schnepel et al., 2015; Reimann et al., 2017). The reduction of multiple cell types and classes into only one excitatory and one inhibitory neuron type per layer in the reference model (Potjans and Diesmann, 2014) implicitly collapses the diversity of neuron morphologies (Amirikian, 2005; Brown and Hestrin, 2009; Hill et al., 2012) which have different spatial connectivity characteristics. Just as for the spatial widths of connections, experimental evidence on distance-dependent delay parameters is also sparse. As reviewed in Section 3.1, the estimates for the conduction speed in unmyelinated nerve fibers as well as for delay offsets are also widely distributed. In addition, experimentally obtained spiking statistics exhibit a high variability, even within the same brain area (Mochizuki et al., 2016). While available experimental data on the typical widths of connections of different types and corresponding conduction delays is inherently uncertain, theoretical neural-field model studies frequently investigate the strong influence of these parameters on the stability of the system (Ermentrout, 1998; Coombes, 2005; Roxin et al., 2005; Bressloff, 2012). In our upscaled model, broader inhibition and larger delays increase the mean per-neuron spike rates and the correlations in all populations, shown in Figure 4D and F. The effect of changing the parameters d_0 and σ_I on \overline{LV} in Figure 4E is again population-specific. The highest \overline{LV} values (above 1.6) are obtained for long delays ($d_0 > 1$), and broader inhibition than excitation in L2/3E; the \overline{LV} remains low (≤ 0.7) in L5I and L6I across the whole parameter space. Figure 4G shows spike rasters of four distinct network states emerging from this parameter space. Short-range inhibition and short delays yield a spatially and temporally homogeneous state (square marker). Increasing the width of inhibition to an intermediate value results in fast global oscillations (diamond marker). For broader inhibition than

Figure 4 (preceding page):

Parameter sensitivity in the upscaled model. A–C Dependency on external rate ν_{ext} and relative weight of inhibition g ($= g_{YX}$ with any inhibitory presynaptic population X). **A** Mean per-neuron spike rates $\bar{\nu}$ for each population (color map with logarithmic scaling). The cross marker denotes the default ‘base parameters’ in this and subsequent panels. **B** Mean coefficients of local variation \overline{LV} for each population, see Equation 33 (color map with linear scaling). **C** Mean Pearson correlation coefficients \overline{CC} between pairs of spike trains for each population, see Figure 3 (color map with linear scaling). **D–F** Same as panels A–C, but for dependency on inhibitory spatial width σ_I and delay offset d_0 . Additional markers refer to parameter combinations used in panels G and H. **G** Spike rasters of selected parameter combinations (showing 3% of all neurons sampled from the full network of size $4 \times 4 \text{ mm}^2$, neurons are sorted as in Figure 2). The symbols in each raster plot legend mark the corresponding locations in the parameter space spanned by d_0 and σ_I (panels D–F). **H** Population-rate power spectral densities (PSD) of selected parameter combinations. The markers correspond to the chosen parameter combinations in panels D–F.

excitation, we observe localized activity spreading outwards (plus marker). Finally, we show an intermediate state (circular marker). These results are in line with predictions from neural-field studies, which indicate that long-range inhibition promotes localized states such as spatially periodic patterns. By contrast, long-range excitation promotes temporally periodic states that can also combine with spatial patterns; see Ermentrout (1998, Chapter 8) and Senk et al. (2018). For a network of spiking neurons, Rosenbaum and Doiron (2014) show that a balanced state of excitation and inhibition requires broader excitation than inhibition. They demonstrate that the balanced state loses stability if excitation is too narrow compared to inhibition, leading to the emergence of spatial activity patterns.

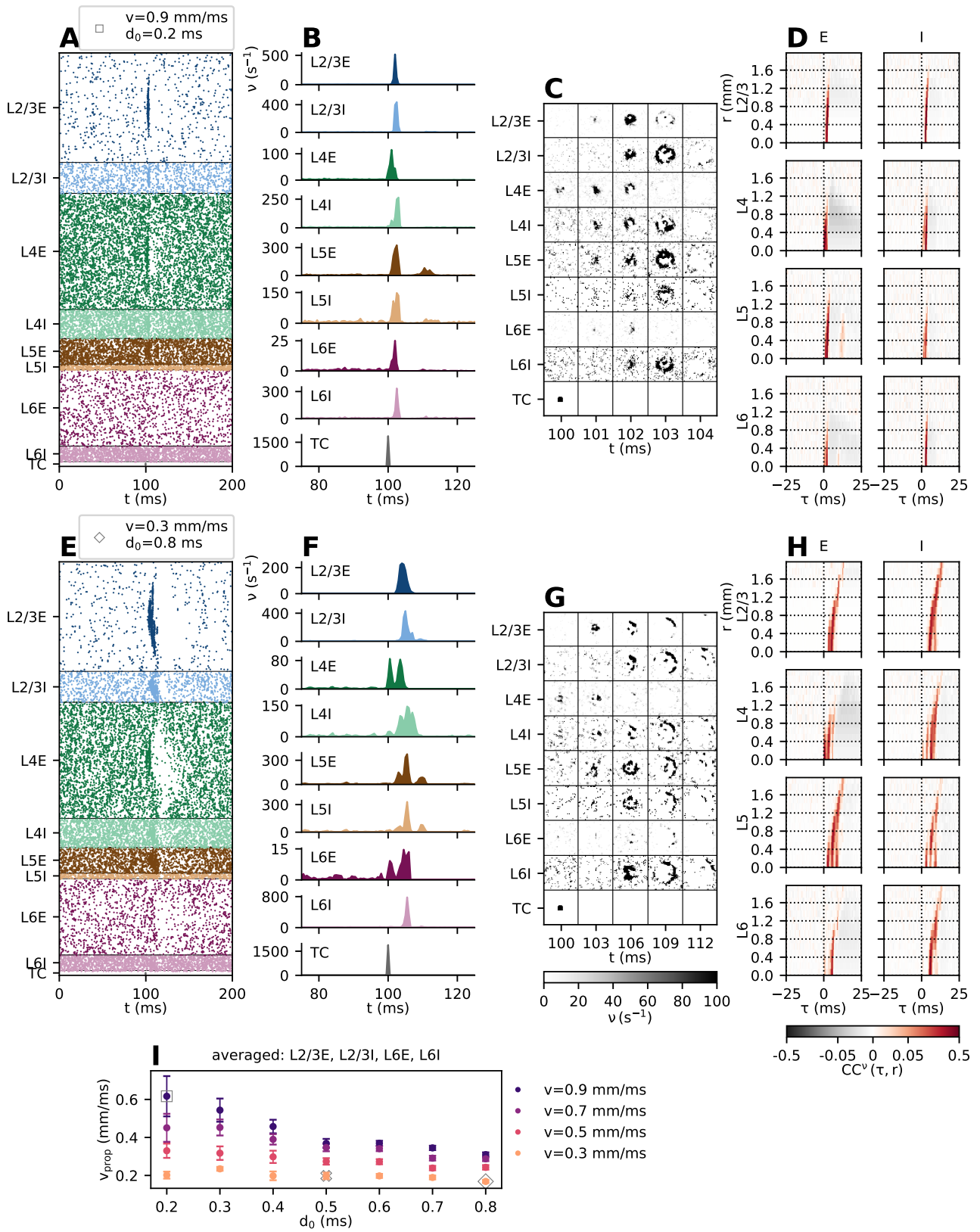
Finally, Figure 4H shows population rate spectra (PSD) varying with the delay offset of the base parameters, $d_0 = 0.5$ ms, and different values for widths of inhibitory connections. While spatially inhomogeneous activity with localized patterns (large σ_I) are manifested as comparatively flat spectra with high power across all frequencies, reducing the spatial width also reduces the overall power, while peaks at the dominant oscillation frequencies emerge. Decreasing σ_I not only reduces amplitudes of the power spectra, the frequency of the high-gamma peak is also gradually shifted to higher values. Both observations can be related to a reduction of the mean inhibitory delay averaged over all connections in the network due to the shorter-range connectivity. The faster inhibitory feedback results in a stronger decorrelation effect that reduces global oscillations (Tetzlaff et al., 2012; Helias et al., 2014). The upward shift of the high-gamma frequency is explained by a shorter time period for the ING mechanism (Bos et al., 2016).

3.2.2 Sensitivity to perturbed parameters during evoked activity

We have so far only considered networks receiving external inputs with stationary rates. Cortical areas are, however, recurrently connected to other parts of cortex and subcortical structures, and receive inputs with large rate fluctuations. We here mimic a stimulation experiment, by activating all thalamic neurons inside a disc of radius R_{TC}^{pulse} around $(x, y) = (0, 0)$ once every time interval of Δt_{TC} (see Table 5 for values). The activation could for example represent a visual stimulation experiment where activity in lateral geniculate nucleus (LGN, or visual thalamus) thalamocortical (TC) projection neurons is evoked by a brief flash stimulus to a part of the visual field (Binguier et al., 1999; Muller et al., 2014), air puffs or mechanical whisker deflections to stimulate whisker barrel cortex (Swadlow et al., 2002; Einevoll et al., 2007), or direct electric or optogenetic stimulation of the thalamocortical pathway (Klein et al., 2016). In its population-specific responses to thalamic pulses, the reference model of Potjans and Diesmann (2014, page 802) exhibits a “handshake principle”, in which the receiving layer inhibits the sending layer as if to signal that it has received the message, so that the sending layer can stop transmitting. We test whether this effect and its strength are preserved in the upscaled model. Furthermore, we derive the propagation speed of evoked spiking activity spreading outward from the center of stimulation. Finally, we test the robustness of the propagation speed to parameter perturbations by varying the conduction speed and the delay offset.

Panels A–D and E–H in Figure 5 show results for two different choices of conduction speed v and the delay offset d_0 . At times prior to a thalamic pulse at $t = 100$ ms, the spiking activities in Figure 5A and E are comparable, and both asynchronous and irregular, despite the different parameterization. However, the effect of the pulse on the network activity is more pronounced in panel E than in panel A according to visual inspection; the initial response lasts longer and the subsequent activity vanishes for tens of milliseconds in different populations. In Hao et al. (2016, Figure 3) a similar suppression period of tens of milliseconds is observed following a single-pulse electrical microstimulation in monkey motor cortex, often followed by a rebound of excitation. In panel E, the effective delay is larger due to the choice of a larger d_0 and a smaller v . In the population-averaged rate histograms of activity within 1 mm^2 in Figure 5B and F, corresponding to the spike rasters in panels A and E, respectively, we highlight the transient network responses by zooming into a smaller time window around the pulse. The strong initial response visible in populations L4E and L6E is expected since the thalamocortical input targets layers 4 and 6 directly (see Table 5). This evoked activity affects the other network populations via recurrent network connections across and within layers. The larger effective delay (panel H) here increases the response latency of the populations, and increases the duration of the responses while their maximum rates in some populations are reduced. The duration of the activation is overall similar to evoked multi-unit activity (MUA) following whisker stimulation as reported by Einevoll et al. (2007). The multiple peaks in the rate histograms in panel D, most prominent in populations L4E, L5E, L5I and L6E, are due to recurrent excitation and inhibition within and across layers. The overall increased delays expectedly break balance, that is, the high temporal correlation of excitatory and inhibitory spiking activity (see, for example, Renart et al., 2010). These results are comparable with Potjans and Diesmann (2014, Figure 10) and Hagen et al. (2016, Figure 7), and we therefore conclude that the upscaling procedure does not fundamentally affect the response of the network to transient external input.

While the population-averaged rate histograms in Figure 5B and F expose the temporal effect of the perturbation of network activity, we next focus on the corresponding spatiotemporal responses. Figure 5C and G show series of snapshots of spatiotemporally binned activity of each population in the full network of size $4 \times 4 \text{ mm}^2$ (similar to Mehring et al., 2003; Yger et al., 2011, Figure 2). The temporal bin size is Δt as in the rate histograms, but we



show snapshots only for selected time points as indicated below the frames. The thalamic pulse is visible only at $t = 100$ ms in the center of the network. The cortical populations respond with a ring-like outward spread of activity which can be described as a traveling wave in contrast to a stationary bump (Muller et al., 2018). The wave travels at a lower speed in the network with larger effective delay (compare selected time points in Figure 5C and G). In order to derive the radial propagation speed of activity evoked by thalamic pulses, we compute the distance-dependent cross-correlation functions (see Section 2.3.6) shown in Figure 5D and H. The maximum value of $CC^\nu(\tau, r)$ shifts faster to larger time lags τ with increasing distances r in panel H compared to panel D, which indicates a lower propagation speed. Figure 5I summarizes the propagation speed estimates v_{prop} as a function of v and d_0 . The estimated propagation speeds increase with increasing conduction speed v and decreasing delay offset d_0 . Estimating the propagation speed in this way from spatially resolved spike trains can help to infer underlying network parameters from experimental data. It is to date difficult to observe wave-like activity on the spiking level (Takahashi et al., 2015). However, model predictions for spiking propagation speeds can be compared with population measures, keeping in mind potential differences between spiking activity and population measures such as the LFP. Both types of signals can reflect propagation along long-range horizontal connections which also includes synaptic processing times, but they are also affected by intrinsic dendritic filtering (Grinvald et al., 1994; Nauhaus et al., 2009; Takahashi et al., 2015; Zanos et al., 2015). Muller et al. (2018) remark that macroscopic waves traveling across the whole brain typically exhibit propagation speeds of 1 – 10 mm/ms similar to axonal conduction speeds of myelinated white matter fibers in cortex, while mesoscopic waves (as considered here) show propagation speeds of 0.1 – 0.8 mm/ms similar to axonal conduction speeds of unmyelinated long-range horizontal fibers within the superficial layers of cortex. For example, LFP ‘waves’ in visual cortex travel with such speeds. Nauhaus et al. (2009) study the propagation of spike-triggered LFPs both in spontaneous activity and with visual stimulation and derive speeds (mean \pm standard deviation) of 0.31 ± 0.23 mm/ms in cat and 0.24 ± 0.2 mm/ms in monkey (both anesthetized). Ian Nauhaus and Carandini (2012) reanalyze the data from Nauhaus et al. (2009) and further report a speed of 0.18 mm/ms in cat and 0.29 mm/ms in monkey for the impulse response of ongoing activity; for data from awake monkey (Ray and Maunsell, 2011) they compute a speed of 0.13 mm/ms. Zanos et al. (2015) measure a speed of 0.31 ± 0.08 mm/ms triggered by saccades in monkey visual cortex. Propagation speeds obtained via voltage-sensitive dye imaging in visual cortex are comparable as well: an average speed of 0.28 mm/ms with a 75% confidence interval of 0.19 to 0.55 mm/ms in cat (Benucci et al., 2007), 0.1 – 0.25 mm/ms in monkey (Grinvald et al., 1994), and a range of 0.25 – 1.35 mm/ms with median \pm standard deviation of 0.57 ± 0.18 mm/ms in monkey (Muller et al., 2014). Estimates from monkey motor cortex are in the same range (Rubino et al., 2006; Takahashi et al., 2015; Denker et al., 2018). For the biologically plausible ranges of delay offsets and conduction speeds tested in the model, $d_0 \in [0.2, 0.8]$ ms and $v \in [0.3, 0.9]$ mm/ms, the resulting propagation speeds are mainly between 0.2 and 0.6 mm/ms. These derived propagation speeds are smaller than the corresponding conduction speeds because propagation through the network includes neuronal integration and the delay offsets. The values in the model cover the range of experimentally measured propagation speeds.

3.3 LFP predictions

We here summarize our findings for the predicted LFP signal across cortical space, with recording geometry similar to a 4×4 mm² Utah multi-electrode array. As in Hagen et al. (2016), the eight cortical network populations spanning layers 2/3, 4, 5 and 6 are expanded into 16 different cell types in order to account for differences in layer specificity of synaptic connections among cell types in a single layer when predicting the LFP. While we here refrain from discussing the detailed derivation of these layer specificities (see Hagen et al., 2016) from available anatomical data (i.e., Binzegger et al., 2004), in Figure 6 we show the reconstructed morphology used for each cell type y in population Y , with compartment counts and occurrences summarized in the table contained within the figure. The cortical layer boundaries and depths are also illustrated, and each morphology is positioned such that the soma is at the center

Figure 5 (preceding page):

Activity evoked by thalamic pulses. **A** Spike raster (showing 3% of all neurons in 4×4 mm², neurons are sorted as in Figure 2). A single thalamic pulse occurs at $t = 100$ ms. **B** Population-averaged rate histogram for neurons within the center disc of 1 mm² with bin size Δt for a time interval around the thalamic pulse shown in panel A. **C** Series of snapshots of spatiotemporally binned activity per population over the whole 4×4 mm² network. **D** Distance-dependent cross-correlation functions between thalamic activation and spatially binned spiking activity $CC^\nu(\tau, r)$ where r is the distance to the center of the network and τ is the time lag. Color maps have a symmetric logarithmic scaling (linear up to threshold of ± 0.05 indicated by ticks in the color bar). Panels A–D are obtained in a network with conduction speed v and delay offset d_0 as indicated in the legend of panel A. **E–H** Same as panels A–D but with parameters as indicated in the legend of panel E. **I** Propagation speed v_{prop} estimated for parameter combinations of conduction speeds and delay offsets and averaged across populations named above the panel; error bars denote standard deviation $\sigma_{v, \text{prop}}$. The same markers correspond to the same parameter combinations throughout this figure. Base parameters are marked with a cross.

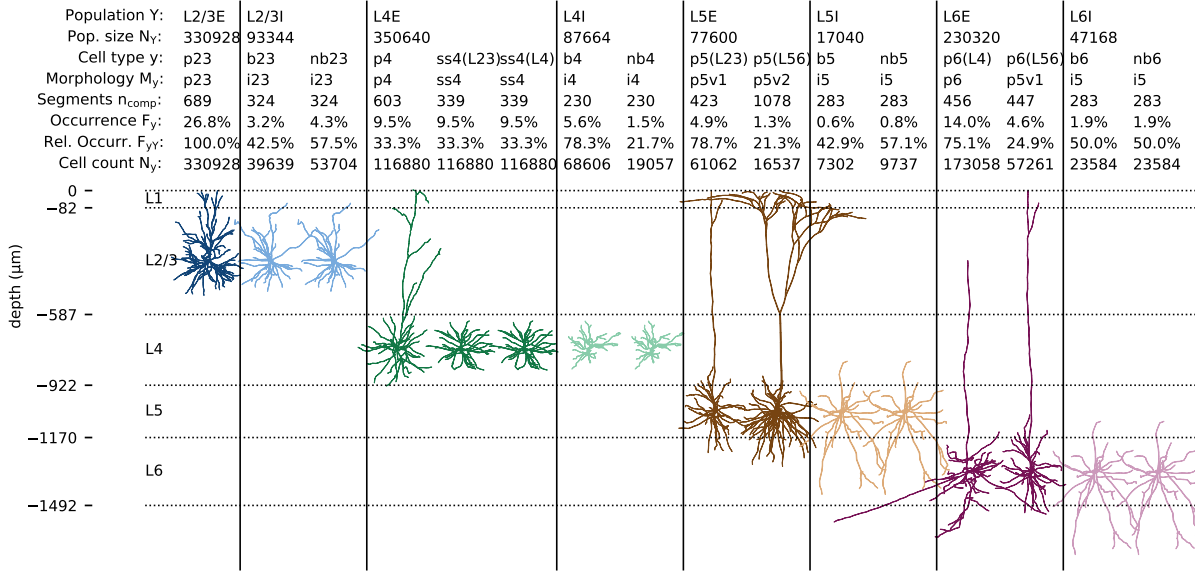


Figure 6: **Cell types and morphologies of the multicompartment-neuron populations.** The 8 cortical populations Y of size N_Y in the $4 \times 4 \text{ mm}^2$ network model are represented by 16 subpopulations of cell type y with detailed morphologies M_y (Binzegger et al., 2004; Izhikevich and Edelman, 2008). Neuron reconstructions are obtained from cat visual cortex and cat somatosensory cortex (source: NeuroMorpho.org by Kisvárdy and Eysel (1992); Mainen and Sejnowski (1996); Contreras et al. (1997); Ascoli et al. (2007); Stepanyants et al. (2008), see Hagen et al., 2016, Table 7). Each morphology M_y is here shown in relation to the layer boundaries (horizontal lines). Colors distinguish between network populations as in Figure 2. The number of compartments n_{comp} , frequencies of occurrence F_y , relative occurrence F_{yY} and cell count N_y are given for each cell type $y \in Y$.

of the corresponding layer. Different cell types belonging to the same population within a layer may have different geometries supporting different layer specificities of synaptic connections. This is the case for example for the p4 pyramidal cell type versus the ss4 spiny stellate cell types that both belong to population L4E of the point-neuron network. Previous modeling studies demonstrate the major effect of the geometry of the morphology on the measured extracellular potential due to intrinsic dendritic filtering of synaptic input (e.g., Lindén et al., 2010; Lindén et al., 2011; Łeski et al., 2013).

The geometry of the recording locations corresponding to the $4 \times 4 \text{ mm}^2$ Utah multi-electrode array is illustrated in Figure 7A. The 100 contact locations denoted by circular markers are positioned on a 10×10 grid with $400 \mu\text{m}$ separation between contact sites. LFPs are computed at the center of layer 2/3 (at $z = -334 \mu\text{m}$). An example LFP signal segment from one chosen channel (channel 68) is shown in panel B, corresponding to the spontaneous activity in our laminar, upscaled point neuron network with ‘base parameters’ introduced above (in Figure 2C and corresponding text). The signal fluctuates with amplitudes similar to experimentally observed spontaneous potentials ($0.1 - 1 \text{ mV}$, Maier et al. (2010); Hagen et al. (2015); Reyes-Puerta et al. (2016)), with occasional larger transients. Further, we estimate from the LFP the underlying current source density (CSD) across space using the so-called kernel CSD method in two dimensions (2DkCSD, Potworowski et al., 2012). The CSD signal is expected to suppress correlations in the LFP resulting from volume conduction, and is therefore less correlated across space as it is taken to reflect the gross in- and outgoing transmembrane currents in vicinity to the recording device (Nicholson and Freeman, 1975; Mitzdorf, 1985; Pettersen et al., 2006, 2008; Potworowski et al., 2012). The LFP and corresponding CSD in general reflect correlations in synaptic input nearby the measurement site and therefore contain contributions from both local and remote neuronal activities. In contrast, the high-frequency ($\gtrsim 100 \text{ Hz}$) part of experimentally obtained extracellular potentials contains information on spiking activity of local neurons. Activity of high-amplitude single neurons may be separated from the background based on classification of their extracellular action-potential waveforms (through ‘spike sorting’, Quiroga, 2007). Even if no units are clearly discernible in the high-frequency part of the signal, a previous biophysical forward-modeling study using biophysically detailed neuron models (Pettersen et al., 2008) shows that the envelope of the rectified high-pass filtered (750 Hz cutoff frequency) signal correlates with the spike rate in the local population of neurons. In this study, this rectified signal is referred to as the multi-unit activity (MUA), which we approximate by summing up all spiking activities of layer 2/3 neurons in $400 \times 400 \mu\text{m}^2$ spatial bins around each contact. The presently used LFP predictions rely on passive neuron models which do not generate spikes; spiking only occurs in the network. The contribution from excitatory and inhibitory spikes are

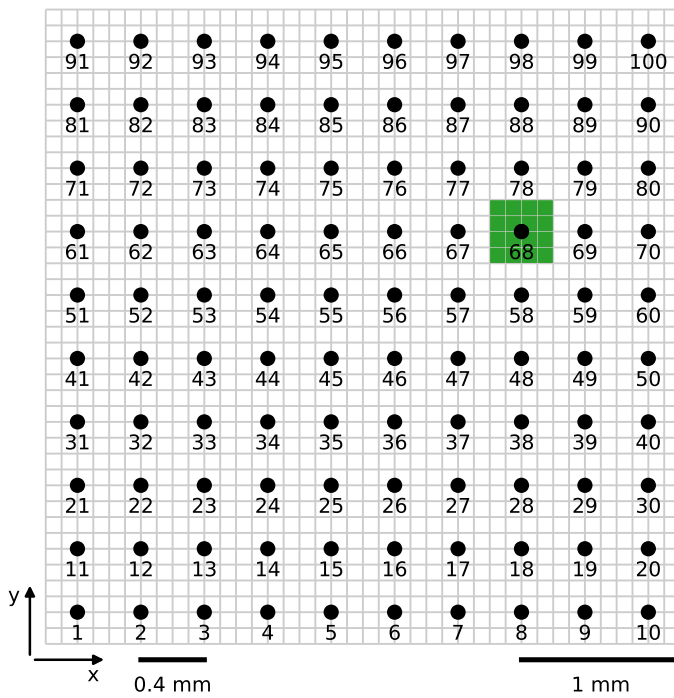
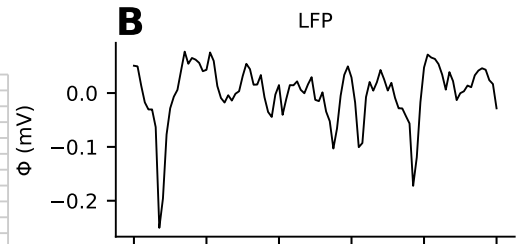
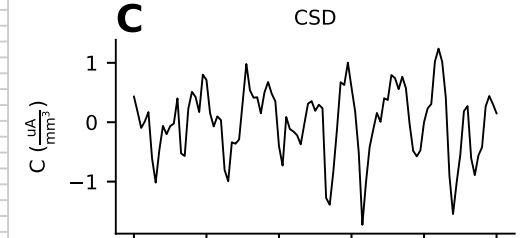
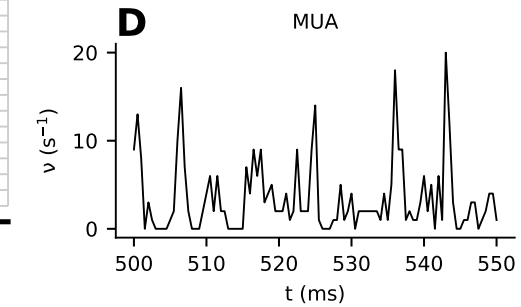
A**B****C****D**

Figure 7: **Illustration of multi-electrode array geometry for LFP, CSD, and MUA predictions.** **A** Extracellular potentials are computed in 10×10 electrode locations denoted by circular markers at the depth corresponding to the center of layer 2/3. The electrode inter-contact distance is $400 \mu\text{m}$. The number under each circular marker denotes the channel number. **B–D** Example LFP, CSD, and MUA from one arbitrarily chosen contact (here channel number 68). The CSD is estimated from the LFP using an inverse method, and the MUA is calculated as the sum of excitatory and inhibitory spike events from layer 2/3 neurons in spatiotemporal bins of duration 0.5 ms and width $400 \mu\text{m}$ around each contact.

weighted identically. One example MUA trace obtained at the same location as the LFP and CSD is shown in Figure 7D. A notable observation is that the MUA signal and its relations to the corresponding LFP and CSD signals are non-trivial.

3.3.1 Distance-dependent correlations of spike trains and LFPs

We next investigate the temporal correlation and coherence with distance for these measures of activity. The observation of weak pairwise spike-train correlations in cortical neuronal networks (for example, Ecker et al., 2010) is seemingly at odds with the typical observation of highly correlated LFPs across cortical space (for example, Nauhaus et al., 2009). We have so far established that the mean pairwise spike-train correlations within populations in our upscaled layered network are typically near zero (Section 3.1), and that the perturbation of key network parameters such as the external rate and delays affect the mean correlation (or ‘synchrony’) in the network (Section 3.2), as well as other measures like regularity (as measured by their mean coefficients of local variation \overline{LV}). It is, however, not clear how this weakly correlated network activity translates into population signals such as the LFP. Previous modeling studies of mechanisms of the spatial reach of the LFP highlight the crucial role of correlation in synaptic inputs to the LFP-generating neurons (Lindén et al., 2011; Łęski et al., 2013). In contrast to these studies, which use input spike trains with Poisson inter-spike statistics, we here account for ongoing network interactions, and realistic numbers of neurons and connections under $4 \times 4 \text{ mm}^2$ of cortical surface using the methods to compute LFPs introduced by Hagen et al. (2016). We thus extend our analysis to distance-dependent correlations in LFP, CSD, MUA, and pairs of spike trains.

For spontaneous spiking activity in the upscaled network (Figure 8A), we compute the LFP (panel C), reconstruct the underlying CSD from the LFP (panel F), and compute the MUA (panel I) across the 100 channel locations in layer 2/3 illustrated in Figure 7A. The network parameters and corresponding network state are those resulting from our upscaling procedure (see Section 2.1.2, base parameters given in Tables 3 and 5). Visual inspection of panel C reveals that the LFP amplitude across channels is typically small ($\lesssim 0.5 \text{ mV}$) as highlighted in Figure 7B with occasional transients which may be seen also on neighboring channels. These transient events presumably result from spatially confined synchronization in the network, but are not seen across every LFP channel as would be the case with globally synchronous network events. The amplitudes observed here are similar to those from the forward-model predictions of LFPs from spontaneous activity in the original 1 mm^2 network model (Hagen et al., 2016, Figure 8M), even if the total number of neurons in the upscaled model is increased by a factor of 16. These similar amplitudes are partially explained by the suppression of strong low-gamma oscillations in the upscaled network using modified connection probabilities. An increase in network synchrony (that is, increased correlations) can otherwise be expected to increase LFP amplitudes overall due to an increased pairwise cross-correlation between single-neuron contributions to the LFP (Hagen et al., 2016). The network upscaling procedure does not obliterate the high- and low-gamma oscillations, which in the LFP spectra result in a large peak around 200 Hz and a small peak around 50 Hz. The network receives background input with a flat power spectrum (driven by a Poisson process with fixed rate) and has no internal sub-circuits capable of generating rate fluctuations or slow oscillations. Hence, the LFP in each channel contains little power towards small frequencies. Another factor explaining the lack of low frequency power is active decorrelation by inhibitory feedback, which is shown to suppress population-rate fluctuations (Tetzlaff et al., 2012; Helias et al., 2014).

We next compute the Pearson product-moment correlation coefficient between all possible pairs of LFP channels, and sort by inter-contact distance (panel E). The mean and standard deviation for each discrete contact separation are shown by the black line and corresponding error bars. Due to the periodic boundary conditions of the network, the longest possible inter-contact distance is $L/\sqrt{2} \approx 2.8 \text{ mm}$. The mean values are well fit by a simple exponential function (red line), with a spatial decay constant of $\sim 0.63 \text{ mm}$ and constant offset of ~ 0.3 . The histogram to the right is computed for all observed correlation coefficients. The correlations in the simulated LFP are lower compared to findings by Nauhaus et al. (2009, Fig. 8) during spontaneous activity in anesthetized macaque (approximately 0.95 at 0.4 mm and 0.75 at 2.4 mm electrode separation, respectively) and cat (approximately 0.93 at 0.4 mm and 0.83 at 2.4 mm electrode separation, respectively). With high-contrast drifting grating type stimuli, however, the correlations between pairs of LFP signals are shown to decrease to values around 0.5 at an electrode separation of 2.4 mm. Also Destexhe et al. (1999) analyze spatial correlations in the LFP of cat suprasylvian cortex during awake and different sleep states, and find mean correlations of approximately 0.6 at 2 mm contact separation in the awake state. These LFP correlations computed from experimental data are highly dependent on the choice of LFP reference which may introduce a shared signal component (which increases correlations), while the present model LFPs are computed with the assumption of an ideal reference electrode at infinite distance from the sources. The point neuron and corresponding LFP model also ignore rate fluctuations in their background input (here represented as Poisson generators with fixed rates) which is another source of spatial correlations. Global fluctuations or shared input correlations in the background input can be expected to increase pairwise LFP correlations (Lindén et al., 2011; Łęski et al., 2013; Hagen et al., 2016).

We next bring our attention to the estimated CSD signal in panel F. By design the chosen CSD estimation method is expected to suppress correlations among channels due to volume conduction by reconstructing the sink/source

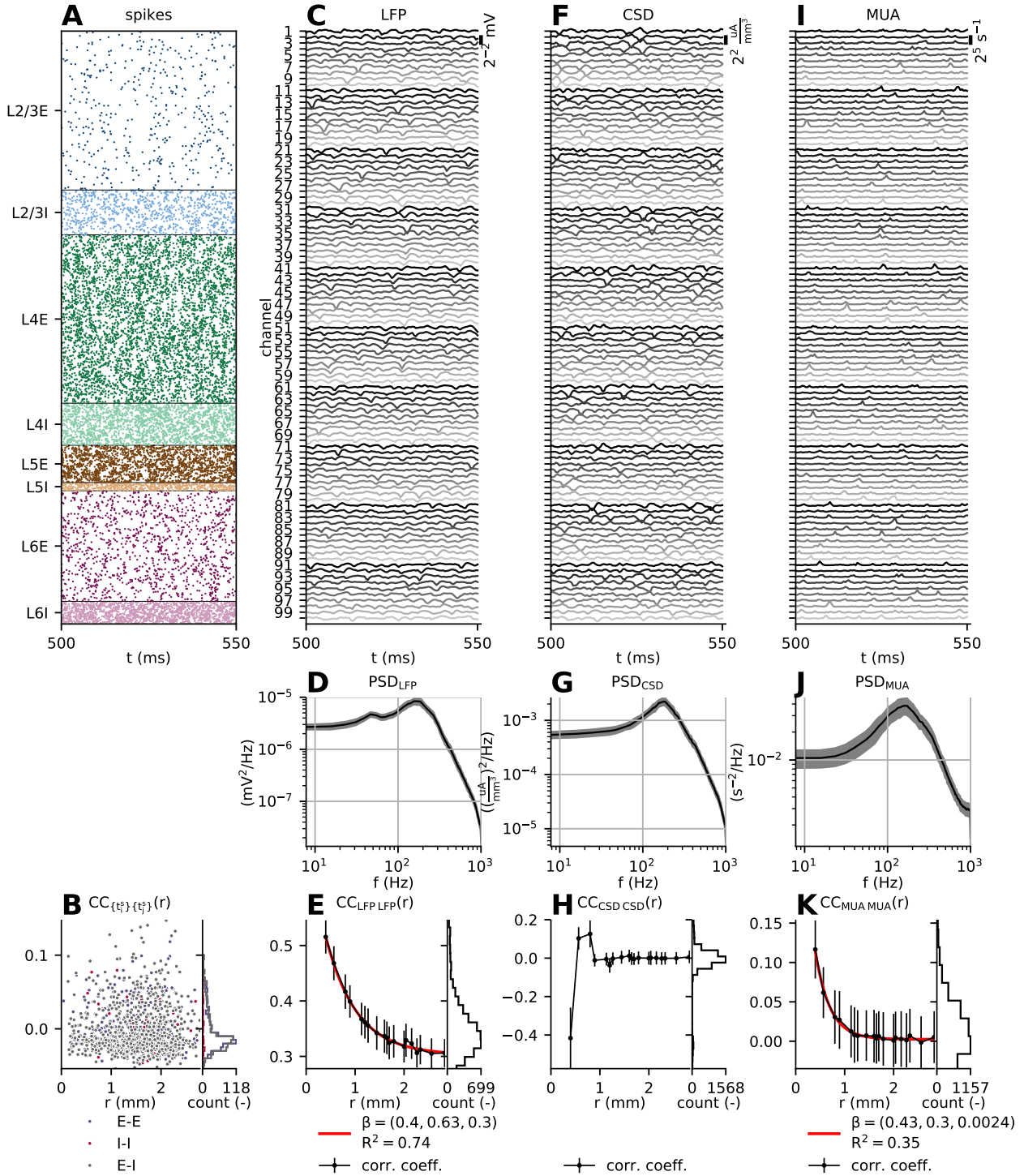


Figure 8: **Spikes, LFP, CSD, and MUA: Raw signals, power spectra, and distance-dependent correlations in L2/3.** **A** Spike raster (showing 10% of all neurons in $4 \times 4 \text{ mm}^2$, neurons are sorted as in Figure 2). **B** Pairwise spike-train correlations computed for pairs of excitatory (E-E, $n = 40$), inhibitory (I-I, $n = 10$) and excitatory and inhibitory (E-I) L2/3 neurons, sorted by inter-neuron distance r . **C** Local field potentials (LFP) across the 10×10 electrode contact points located at the center of layer 2/3, each separated by $400 \mu\text{m}$ in the lateral directions. **D** LFP power spectrum averaged over channels (black line). The gray area denotes the average spectrum plus/minus one standard deviation. **E** Pearson correlation coefficient between pairs of LFP signals as function of separation between channels. The black line shows the mean at each unique separation, whiskers denote one standard deviation. The red line shows the least-square fit of an exponential function to all values. The coefficient of determination (R^2) is given in the legend. **F** Current-source density (CSD) estimates from LFPs shown in panel C, calculated using the kCSD method in 2D. **G** CSD power spectrum (mean \pm one standard deviation). **H** Similar to panel E but for CSD signals, minus fit to exponential function. **I** Multi-unit activity (MUA) approximated as the bin-wise spike rates of layer 2/3 excitatory and inhibitory point neurons, calculated using a spatial bin width $\Delta h = 400 \mu\text{m}$. **J** MUA power spectrum (mean \pm one standard deviation). **K** Similar to panel E but for MUA signals.

pattern underlying the LFP (Nicholson and Freeman, 1975; Mitzdorf, 1985; Pettersen et al., 2006, 2008; Potworowski et al., 2012). This can, for example, allow the identification of loci of strong synaptic activity in experimental LFP data, which may be generated locally or due to some external drive. A brief inspection of the CSD traces computed from the model LFP reveals that ‘standout’ LFP events (e.g., in channel 31 at 525 ms) result in fluctuations in the corresponding CSD, but the traces appear overall more variable than the LFP. Just as for the LFP, we show the power spectra (panel G) and pairwise correlation coefficients with distance (panel H). In contrast to the LFP spectra, the low-gamma peak around 50 Hz is not present in the CSD spectra, but the high-frequency peak remains. The overall positive correlations observed for the LFP are largely canceled for the CSD. The CSD signals are typically anti-correlated with mean around -0.4 at the shortest electrode separations (0.4 mm), and then weakly correlated (~ 0.1) up to 1 mm. This CSD anti-correlation across proximal channels is expected, as a fraction of capacitive and resistive (‘leaky’) transmembrane return currents of synaptic input currents exits in vicinity to the synapse site and at the soma. The return currents are affected by intrinsic dendritic filtering (Lindén et al., 2010) throughout each individual LFP-generating neuron morphology. Our multicompartment cells are effectively treated as closed electric circuits and the basic principle of charge conservation must apply (see, for example, De Schutter and Van Geit, 2009). The correlations between channels are negligible beyond 1 mm electrode separation. This negligible correlation at greater distances reflects in part that dendrites of each morphology (cf. Figure 6) are mostly confined within $\sim 300 \mu\text{m}$ in the lateral directions, and that local spontaneous network interactions for this particular network parameterization do not readily propagate across space. It is important to point out that the CSD estimate (cf. Section 2.3.3) is based on LFPs computed at a single depth only, and would change if LFPs across all depths were taken into account.

As an approximation to the so-called multi-unit activity (MUA) signal, we sum up spiking activity in layer 2/3 in the vicinity of each LFP contact point (cf. Section 2.3.4), resulting in the signals in Figure 8I. Similar to the computed LFP and CSD signals, we compute power spectra (panel J) and distance-dependent pairwise correlations among MUA signals (Figure 8K). In contrast to pairwise spike-train correlations (Figure 8B), a sharply decaying distance dependency is observed, which is well fit by an exponential function with spatial decay constant of $\sim 0.30 \text{ mm}$ and vanishing offset from zero at greater distances. This sharp decay contrasts with the longer spatial decay constant observed for the LFP, and the anti-correlation between neighboring sites as observed for the CSD does not occur. These differences reflect that the LFP and CSD are measures resulting from synaptically driven transmembrane currents, while the MUA is a measure of the network spiking activity resulting from said synaptic input. Similar to the CSD spectra, the low-gamma oscillation around 50 Hz is not seen, while the high-gamma oscillation around 200 Hz is pronounced.

3.3.2 Spatial coherence of local field potential is band-passed

So far we have established that the model LFP is highly correlated with distance in qualitative agreement with experimental findings, while the corresponding CSD and MUA signals are hardly correlated beyond electrode separations of $\sim 1 \text{ mm}$. We next extend this analysis to the frequency domain by considering distance-dependent coherences. This step is mainly motivated by two experimental observations: LFP coherence across channels depends on inter-electrode distance as described by Jia et al. (2011); Srinath and Ray (2014), and a recent study by Dubey and Ray (2016) shows that the ‘spatial spread’ of LFP has band-pass properties in the gamma range (60–150 Hz). Another modeling study (Łęski et al., 2013) extends the study of LFP ‘reach’ by Lindén et al. (2011) to distance-dependent coherences, showing that dendritic filtering (Lindén et al., 2010) introduces a low-pass effect on the LFP reach of uncorrelated synaptic input currents with an approximately white power spectrum. In contrast to these latter modeling studies, our combined point-neuron network and LFP-generating setup allows accounting for weakly correlated spiking activity in the network, at realistic density of neurons and connections.

From its spectra (Figure 8D) we infer that most of the variance in the spontaneous LFP data is due to a high-frequency gamma oscillation above 200 Hz in the network due to the ING mechanism present in each layer (Bos et al., 2016). In Figure 9A we show the mean coherences $\langle \gamma_{\text{LFP-LFP}} \rangle(f)$ between individual pairs of LFP signals from channels separated by a distance $r = \{0.4, 0.8, 1.2, 1.6, 2.0\} \text{ mm}$. While the coherence is, as expected, highest for the lowest frequencies ($\lesssim 10 \text{ Hz}$) at all separations, it drops quickly for frequencies $f \approx 20 \text{ Hz}$. For the shortest separation (0.4 mm), the coherence is around 0.35 at this frequency, and increases to ~ 0.5 in the low-gamma range (around 50 Hz). Broader peaks in the coherence with magnitudes around 0.3 and 2 are also seen for 100–150 Hz and 250–300 Hz, respectively. Beyond this range, the coherence drops to around 0.1. The coherence across all frequencies is further reduced for increased separations, but at 2 mm separation it still drops to the same value of ~ 0.1 at high frequencies. These model observations resemble coherences computed for experimental LFP data during stimulus conditions (Srinath and Ray, 2014, Figure 1A). There, a peak in low-gamma coherence around 40 Hz is seen for distances up to 4 mm in two different subjects. Also an increase in coherence is seen for frequencies around 80 Hz. The baseline coherence (no visual stimulus) shows no increase in the gamma range of frequencies, except for sharp peaks seen at 100 Hz due to the CRT display frequency and 120 Hz due to the second harmonic of noise (Srinath and Ray, 2014). This lack of gamma peaks of physiological origin differs from our model predictions. We therefore conclude that the model LFP coherence more closely resembles the stimulus-driven LFP, but we note also that a baseline stationary thalamocortical activation level is assumed in the reference network (Potjans and

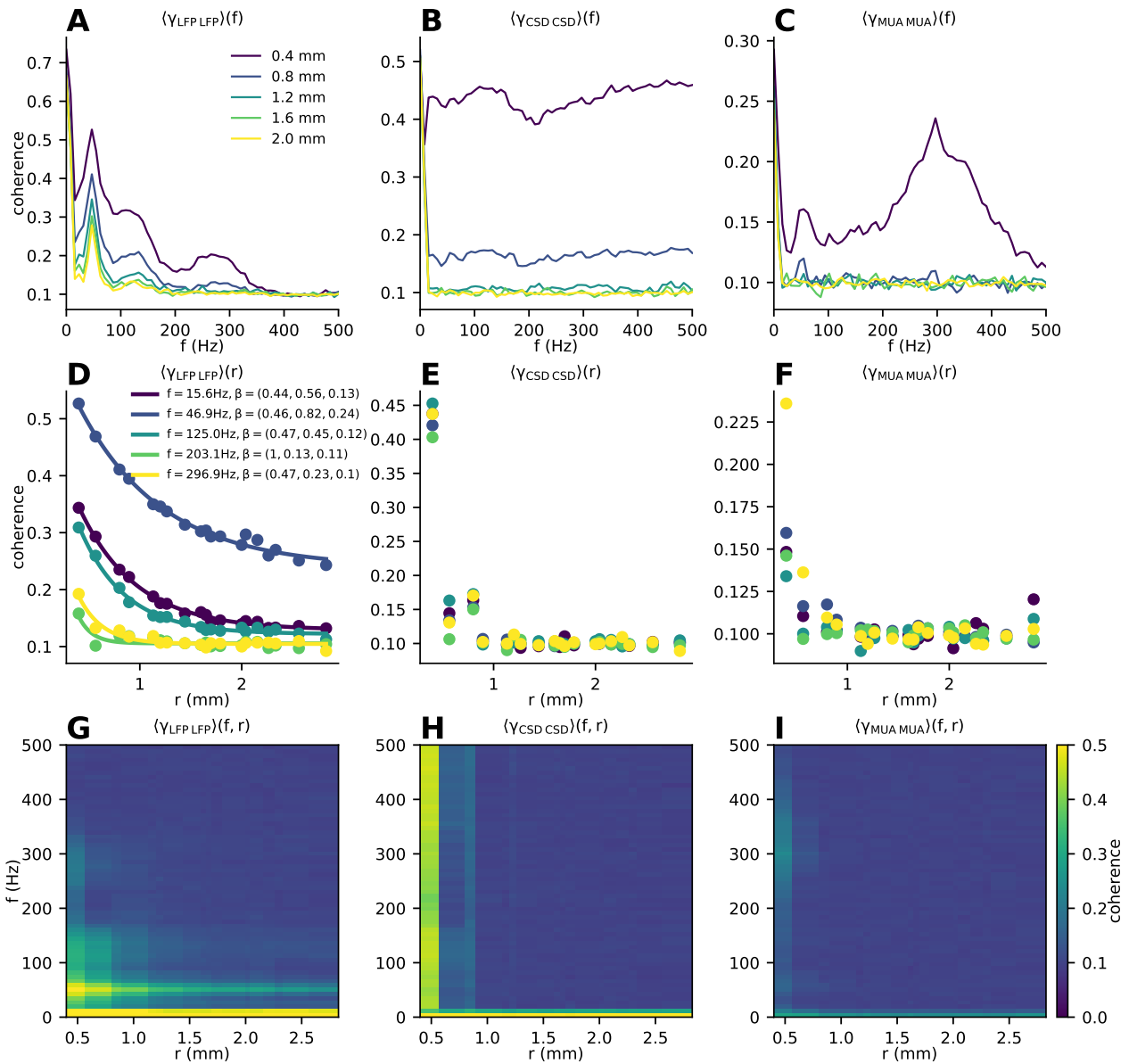


Figure 9: **Distance dependency of LFP, CSD, and MUA coherences in L2/3.** **A** Pairwise LFP coherences as function of frequency for different distances (color-coded) between electrode contacts r , averaged over pairs with identical electrode separation. **B** Similar to panel A but computed using the reconstructed CSD signal estimates at each electrode. **C** Similar to panel A and B but computed using the MUA signal at each electrode. **D** Mean LFP coherences as function of distance between electrode contacts for different frequencies (color-coded) with exponential fit to mean values ($R^2 = \{1, 0.99, 0.99, 0.70, 0.93\}$ for $f = \{15.6, 46.9, 125.0, 203.1, 296.9\}$ Hz, respectively) **E, F** Mean CSD, and MUA coherences as function of distance between electrode contacts for different frequencies (color-coded). **G–I** Color image plot of mean LFP, CSD, and MUA coherences as function of frequency and electrode separation.

Diesmann, 2014). This baseline activation enters the $K_{X,\text{ext}}^{\text{th}}$ parameter for populations $X \in \{\text{L4}, \text{L6}\} \times \{\text{E}, \text{I}\}$ also in the upscaled network. The corresponding mean-field theory (Bos et al., 2016) identifies sub-circuits located in and across layers 2/3 and 4 as the origins of the low-gamma oscillations. Therefore, a reduced external drive to layer 4 (by turning off the baseline thalamic activation altogether) should reduce the magnitude of this intrinsically generated oscillation and consequently reduce the corresponding spatial LFP coherence. An opposite effect on coherence can be expected by increasing the thalamocortical drive in the model. At present we do not pursue this possibility further. We also note that our LFP coherence is smaller than the comparable experimental values (Srinath and Ray, 2014), but see also Jia et al. (2011) and Dubey and Ray (2016). This smaller coherence underlies the reduced correlation with distance noted above which is likely due to the lack of temporally modulated input and intrinsically generated low-frequency fluctuations, and the use of an ideal reference. Some of these differences may also result from the fact that these experimental studies rely on the multitaper method (Thomson, 1982) in order to compute coherences while we use Welch's average periodogram (see Section 2.3.6), and that the experimental data have longer durations than our chosen simulation period of $T_{\text{sim}} = 5$ s.

We next investigate the distance dependency of coherences for different frequencies. Dubey and Ray (2016) show an apparent band-pass effect in the LFP, in that the phase coherence across sites is increased and decays more slowly with distance in the gamma range compared to higher and lower frequencies. In Figure 9D we show the LFP-LFP coherences as functions of distance for different frequencies f , averaged over values computed for identical separation of channels. We also show the corresponding least-square fit to exponential functions, in order to investigate whether or not this model reproduces the experimentally observed band-pass effect. Indeed, we find for $f \approx 46.9$ Hz, which is at the center of the low-gamma peak in panel A, an elevated coherence with longer spatial decay constant ($\lambda = 0.82$ mm) than for frequencies where the overall coherence is reduced, such as $f = 15.6$ Hz ($\lambda = 0.56$ mm) and $f = 203.1$ Hz ($\lambda = 0.13$ mm). In the high-gamma band ($f = 296.9$ Hz) we again note a comparatively quick decay ($\lambda = 0.23$ mm) in coherence, which may reflect that the network interactions underlying the generation of this oscillation frequency remain local. In panel G we show the same data as displayed in panel A and D for all frequencies up to 500 Hz and average for each distance up to 2.8 mm. As implied by the above findings, the low-gamma peak in the coherence near 50 Hz is seen at all distances.

In a similar manner we compute distance-dependent coherences for the CSD (panels B,E,H) and MUA (panels C,F,I). The CSD shows only a weak frequency dependence in its coherence at all tested distances (panel B). The coherence is ~ 0.4 for a contact separation of 0.4 mm, and drops to levels below 0.2 at greater distances. The MUA coherence, however, is increased for the shortest distances (0.4 mm) around the high-frequency range of the high-gamma oscillation (~ 300 Hz) as shown in panel C, but the coherence is at the baseline level at all greater distances.

4 Discussion

The present work investigates a multi-layer point-neuron network model covering 4×4 mm² of cortical surface at realistic neuron and connection density, amounting to $\sim 1.2 \cdot 10^6$ neurons and $\sim 5.5 \cdot 10^9$ synapses. The model accounts for spiking activity across excitatory and inhibitory neurons in layers 2/3, 4, 5, and 6 and one external thalamocortical population, as well as local field potentials (LFP). The 4×4 mm² area covered by the model is similar to the one covered by a 10×10 Utah multi-electrode array commonly used for electrophysiological measurements in vivo in different cortical areas and species. The model is a laterally extended version of the cortical microcircuit under 1 mm² of cortical surface by Potjans and Diesmann (2014), but in contrast to this reference network the upscaled network accounts for distance-dependent connection probabilities and delays. The biophysics-based LFP predictions rely on the hybrid scheme for LFP predictions in point-neuron networks by Hagen et al. (2016), which is here modified to account for spatially structured networks. Earlier work has shown that correlations are perturbed in downscaled networks (van Albada et al., 2015). The LFP reflects the fluctuations caused by network correlations and depends also on the spatial organization of networks (see, for example, Hagen et al., 2016). Therefore, the development of biophysical network models that incorporate the full density of connections as well as the spatial organization of the observed system is crucial to aid the interpretation of the corresponding experimental data.

Our upscaling procedure preserves the overall features of activity in the reference network. This includes a stable network state with asynchronous and irregular spiking activity for the different neuron populations, distributed firing rates across neurons, spike trains with variability in agreement with observed activity in sensory cortex, weak pairwise spike-train correlations, and population firing rate spectra with peaks in the low-gamma range (40 – 80 Hz) and high-gamma range (200 – 300 Hz). Around this stable state, we investigate the effect of varying key network parameters, namely the weight of inhibitory connections and the external drive, as well as the width of inhibitory connection profiles and the minimum delays. We find that a strong external drive with reduced inhibitory feedback results in high synchrony, that conduction delays strongly affect the formation of temporal oscillations, and that wide inhibition results in spatial instabilities. Furthermore, the model exhibits spatially spreading activity evoked by thalamic pulses comparable to experiments with a brief flash stimulus to a part of the visual field in terms of the radial propagation speed of the evoked responses. Finally, the model accounts for spatially correlated and coherent LFPs even during

spontaneous network activity when its pairwise spike-train correlations are low on average. LFP coherences are distance-dependent with a slower spatial decay around the frequency of the 50 Hz low-gamma oscillation compared to other frequencies, resulting in an apparent band-pass filter effect on the LFP coherence.

4.1 Comparison with other studies

To our knowledge, this computational study is the first to simultaneously account for both spiking activity and population activity measures such as the LFP in a layered network model that covers several square millimeters of cortical surface at the full density of neurons and synaptic connections. Compared to experimentally reported cortical neuron densities of $\sim 10^5$ neurons/mm² (see, for example, Herculano-Houzel, 2009; Ribeiro et al., 2013), other studies of laminar point-neuron networks with distance-dependent connections (Mehring et al., 2003; Yger et al., 2011; Voges and Perrinet, 2012; Rosenbaum and Doiron, 2014; Keane and Gong, 2015; Schnepel et al., 2015; Pyle and Rosenbaum, 2017; Rosenbaum et al., 2017) either rely on reducing the overall size of the network’s geometry, reduce the neuron densities per cortical area, consider only one layer of excitatory and inhibitory neurons, or collapse all cortical layers into one. Tomsett et al. (2014) also incorporate LFP predictions from a recurrently connected network of $\sim 10^5$ multicompartiment neurons, but consider only a thin cortical slice across layers similar to in vitro experiments. While reduced cell and connection counts speed up simulations, state-of-the-art point-neuron simulation software scales nearly linearly up to $\sim 10^9$ neurons (Kunkel et al., 2017; Jordan et al., 2018). Hence, simulations of networks with $\sim 10^6$ neurons such as ours can be executed routinely on high-performance computing facilities.

We here choose to start from a previously published model of the cortical microcircuit by Potjans and Diesmann (2014). In increasing the model size, the choice of scaling procedure is critical. van Albada et al. (2015) show that the reducibility (downscaling) of randomly connected asynchronous networks is fundamentally limited if both spike rates and second-order statistics (correlations) are to be preserved. Their proposed scaling rules adjust the amplitudes of synaptic currents and mean and variance of noisy background input to the decreasing numbers of synapses. However, upscaling is different. In the microcircuit model each neuron receives a realistic number of synapses, originating either from within the circuit or attributed to the background. Increasing the network size necessarily decreases the probability for two neurons to be connected. The consideration of spatial organization, however, preserves a certain level of local recurrence while the total network size is growing. Consequently, our upscaling procedure works without the need to adjust the amplitudes of synaptic currents of the reference network. The distance-dependent connectivity results in modified in-degrees of recurrent network connections and noisy background input such that the mean input to each neuron is preserved, but not its variance. As demonstrated here, the activity statistics of neurons in a 1 mm² patch in the upscaled network is comparable to the statistics of the reference network. This retrospectively validates the decisions made in the construction of the microcircuit model by Potjans and Diesmann (2014).

The modeled LFP has amplitudes in agreement with spontaneous LFP amplitudes observed experimentally between 0.1 – 1 mV (see, for example, Maier et al., 2010; Hagen et al., 2015; Reyes-Puerta et al., 2016). The LFP spectra reveal a strong ongoing oscillation at high frequencies, in the 200 – 300 Hz range, and around 50 Hz. Spectra of spontaneous potentials in visual cortex do not typically reveal strong oscillations at these frequencies, but elevated LFP gamma power in the 30 – 80 Hz range is frequently reported during stimuli (Jia et al., 2011; Ray and Maunsell, 2011; Berens et al., 2008; Xing et al., 2012; Veit et al., 2017; Katzner et al., 2009; Jia et al., 2013b; Hadjipapas et al., 2015). A functional role in computation and synchronization between areas has therefore been hypothesized (Ray and Maunsell, 2010; Jia et al., 2013a; Buzsáki and Wang, 2012). The strong high-frequency oscillations here result from short interneuron conduction delays (Bos et al., 2016). Low frequencies are lacking in our spontaneous LFP as our network receives external drive with a stationary rate, does not intrinsically generate slow rate fluctuations, and is subject to active decorrelation (Tetzlaff et al., 2012), as well as due to the assumption of an ideal reference at infinite distance from the source. Nevertheless, the model produces highly correlated LFPs with a distance dependence compatible with experimental observations (Destexhe et al., 1999; Nauhaus et al., 2009). The model also reproduces elevated coherences in the low-gamma band as seen during visual stimulation (Jia et al., 2011; Srinath and Ray, 2014). The slower spatial decay for frequencies around 50 Hz in the model is consistent with a recent report of increased spatial LFP ‘reach’ analogous to a spatial band-pass filter effect in the low-gamma band (Dubey and Ray, 2016).

4.2 Possible model refinements

The upscaled model establishes local connections with a Gaussian decay of connection probabilities up to a radius of 2 mm. However, pyramidal neurons can develop long horizontal axons spanning several millimeters in addition to local axonal branching. In cat and monkey visual cortex, these connections are typically clustered or patchy and connect neurons with similar orientation tuning (Livingstone and Hubel, 1984; Gilbert and Wiesel, 1989; Bosking et al., 1997; Tanigawa et al., 2005; Buzás et al., 2006; Binzegger et al., 2007). In contrast, the visual cortex of rodents exhibits a salt-and-pepper layout without patchiness, but still some longer-distance connections (Ohki and Reid, 2007; Laramée and Boire, 2015). Although less common, subsets of inhibitory interneurons can also exhibit long-range connections (McDonald and Burkhalter, 1993). Voges and Perrinet (2012) assess the influence of different types of

remote connections (none, random, or patchy) on the network activity of a 2D single-layer network, and conclude that the fraction of local versus remote connections is crucial for the resulting network dynamics, irrespective of the detailed spatial arrangement of remote connections.

For the type of model development conducted here, comprehensive datasets with detailed (distance-dependent) connection probabilities are mostly unavailable for all possible pairs of pre- and postsynaptic neuron types and different cortical layers. Some exceptions exist (for example, Binzegger et al., 2004), but most connectivity studies focus on specific connections, and due to differences in experimental methods, results may be difficult to compare and reconcile; see, for example, Schnepel et al. (2015, Supplementary Material) on the limitations of their photostimulation technique and Stepanyants et al. (2009) on truncated connections in brain slices. Neuron morphology appears to provide a valid first approximation for the distance dependency of connections (Amirikian, 2005; Brown and Hestrin, 2009; Hill et al., 2012; Rees et al., 2016), but the overlap between dendrites and axons alone does not explain connectivity patterns, due to target neuron-type specificity (Potjans and Diesmann, 2014), specificity at the level of individual neurons (Kasthuri et al., 2015), and preferential locations of dendritic spines and synaptic boutons on connected neurons (Ohana et al., 2012). We make the conservative choice to let the spatial widths of connections and shape of postsynaptic potentials depend only on the presynaptic neuron type. Our hope is that the algorithmic approach pursued within consortia such as the Blue Brain Project (Reimann et al., 2015; Markram et al., 2015) and the Allen Brain Institute (Kandel et al., 2013) will provide more accurate neuronal connectomes of different brain regions across species in the future, including their distance dependencies (as in, for instance, Reimann et al. (2017) for rat somatosensory cortex).

Activity in finite-sized laminar networks is subject to effects that depend on the choice of boundary conditions. Periodic boundary conditions are frequently used in 1D networks (ring networks) (Roxin et al., 2005; Kriener et al., 2014; Rosenbaum and Doiron, 2014) and in 2D networks with torus connectivity (Mehring et al., 2003; Yger et al., 2011; Voges and Perrinet, 2012; Rosenbaum and Doiron, 2014; Keane and Gong, 2015; Schnepel et al., 2015; Pyle and Rosenbaum, 2017; Rosenbaum et al., 2017) as also used here for the upscaled models. The model of a cortical slice by Tomsett et al. (2014) incorporates connections only within the confines of the modeled slice, but we consider networks that are part of a larger system (the intact brain). An advantage of periodic boundaries is the simplifying assumption that cortex is homogeneous and isotropic, that is, the connectivity of a neuron is independent of its location in the network. One disadvantage is that the maximal distance for connections is only $L/2$ for a ring domain with circumference L , or $L/\sqrt{2}$ for a square domain with side length L . Here, we restrict connections to a radius $R = L/2$. Another disadvantage is that propagating activity may travel across the boundary and directly influence its own propagation, resulting in for example wave-front annihilation (Muller et al., 2018). An option to suppress such effects would be to simulate a larger network and to sample only the activity of neurons across a smaller domain. In Figures 2 and 3, we extract activity of neurons within a center disc of 1 mm^2 . The network could be further upscaled, for example to cover a full cortical area. The lateral size of the unfolded cat striate cortex in one hemisphere is larger by a factor of almost 25 than the currently simulated upscaled network of 16 mm^2 , estimated in the range of $310 - 400 \mu\text{m}$ (Tusa et al., 1978; van Essen and Maunsell, 1980; Olavarria and Sluyters, 1985; Anderson et al., 1988). Striate cortex in macaque monkeys is even two to four times larger than in cats (van Essen and Maunsell, 1980). Networks of a full cortical area could also address the effects of borders to adjacent cortical areas. Anatomical borders between distinct areas are shown to affect wave propagation (Xu et al., 2007; Muller et al., 2014).

Spontaneous activity in our models is driven by uncorrelated external inputs with a fixed rate and Poisson statistics, to represent missing connections from remote and neighboring cortices, subcortical structures, and sensory inputs. Ongoing work aims to account for the structure of one hemisphere of macaque vision-related cortex in a spiking model (Schuecker et al., 2017; Schmidt et al., 2018). Mutual interactions between recurrently connected areas can be expected to profoundly affect their input statistics in terms of rates, spectra, and correlations. Furthermore, we simulate evoked potentials by short thalamic pulses of activity, but sensory cortex receives continuously varying inputs. Ever more detailed models of, for example, the response properties of relay cells in visual thalamus are emerging (Martínez-Cañada et al., 2018), representing naturalistic image or movie stimuli to cortical models similar to ours.

Activity statistics such as distributions of correlations depend on simulation length (Tetzlaff et al., 2008). Here, we consider 5 s simulations, but experimental recordings are often longer (for example, Pan et al., 2013; Chu et al., 2014b,a). Future work can address how greater simulation durations affect the activity statistics, and their convergence across time.

In terms of signal predictions, the tool LFPy (LFPy.rtdf.io) embedded in the presently used hybrid scheme (Hagen et al., 2016), facilitates the calculation of current dipole moments of individual neurons and associated contributions to electroencephalographic (EEG) signals and magnetoencephalographic (MEG) signals as recorded on the surface of the head (Hämäläinen et al., 1993; Nunez and Srinivasan, 2006; Hagen et al., 2018). Forward-model predictions of macroscopic signals like EEG and MEG are thus a tempting proposition, in particular under the consideration of mutual interactions between areas. Among other applications, this could provide an avenue towards a mechanistic model and understanding of visually evoked potentials (Sokol, 1976).

4.3 Significance of work

The present work represents a stepping-stone for understanding experimental data obtained by multi-electrode arrays that cover several square millimeters of cortical space. While the model description is highly reduced, it simultaneously accounts for spiking activity and LFPs and thereby enables a multi-scale comparison with corresponding experimental data. At the same time, its simplicity makes mathematical analysis in terms of mean-field and neural field theory viable (Bos et al., 2016; Senk et al., 2018). Our hope is that the model facilitates a more principal understanding of the dependence of spike correlations on distance, spatially coherent and correlated LFPs, spike-LFP relationships, and emergent spatiotemporal patterns such as waves. The article describes not only a particular network model but a fully digitized “integrative loop”. We therefore envision the model as a starting point and building block for future work iteratively modifying parameters and adding further constraints to generate predictions for the activity of specific brain areas.

References

- Abeles M (1991) *Corticonics: Neural Circuits of the Cerebral Cortex* Cambridge University Press, Cambridge, 1st edition.
- Amirikian B (2005) A phenomenological theory of spatially structured local synaptic connectivity. *PLoS Comput. Biol.* 1:e11.
- Andersen P, Silfvenius H, Sundberg SH, Sveen O, Wigström H (1978) Functional characteristics of unmyelinated fibres in the hippocampal cortex. *Brain Res.* 144:11–18.
- Anderson PA, Olavarria J, Sluyters RCV (1988) The overall pattern of ocular dominance bands in cat visual cortex. *J. Neurosci.* 8:2183–2200.
- Ascoli GA, Donohue DE, Halavi M (2007) NeuroMorpho.org: A central resource for neuronal morphologies. *J. Neurosci.* 27:9247–9251.
- Benucci A, Frazor RA, Carandini M (2007) Standing waves and traveling waves distinguish two circuits in visual cortex. *Neuron* 55:103–117.
- Berens P, Keliris GA, Ecker AS, Logothetis NK, Tolias AS (2008) Comparing the feature selectivity of the gamma-band of the local field potential and the underlying spiking activity in primate visual cortex. *Front. Syst. Neurosci.* 2:1–9.
- Berg-Johnsen J, Langmoen IA (1992) Temperature sensitivity of thin unmyelinated fibers in rat hippocampal cortex. *Brain Res.* 576:319–321.
- Binzegger T, Douglas RJ, Martin KAC (2004) A quantitative map of the circuit of cat primary visual cortex. *J. Neurosci.* 24:8441–8453.
- Binzegger T, Douglas RJ, Martin KAC (2007) Stereotypical bouton clustering of individual neurons in cat primary visual cortex. *J. Neurosci.* 27:12242–12254.
- Börgers C, Kopell N (2003) Synchronization in networks of excitatory and inhibitory neurons with sparse, random connectivity. *Neural Comput.* 15:509–538.
- Börgers C, Kopell N (2005) Effects of noisy drive on rhythms in networks of excitatory and inhibitory neurons. *Neural Comput.* 17:557–608.
- Bos H, Diesmann M, Helias M (2016) Identifying anatomical origins of coexisting oscillations in the cortical micro-circuit. *PLoS Comput. Biol.* 12:e1005132.
- Bosking WH, Zhang Y, Schofield B, Fitzpatrick D (1997) Orientation selectivity and the arrangement of horizontal connections in tree shrew striate cortex. *J. Neurosci.* 17:2112–2127.
- Boucsein C, Nawrot M, Schnepel P, Aertsen A (2011) Beyond the cortical column: abundance and physiology of horizontal connections imply a strong role for inputs from the surround. *Front. Neurosci.* 5:32.
- Bressloff PC (2012) Spatiotemporal dynamics of continuum neural fields. *Journal of Physics A: Mathematical and Theoretical* 45:033001.
- Binguier V, Chavane F, Glaeser L, Frégnac Y (1999) Horizontal propagation of visual activity in the synaptic integration field of area 17 neurons. *Science* 283:695–699.

- Brown SP, Hestrin S (2009) Intracortical circuits of pyramidal neurons reflect their long-range axonal targets. *Nature* 457:1133–1136.
- Brunel N (2000) Dynamics of sparsely connected networks of excitatory and inhibitory spiking neurons. *J. Comput. Neurosci.* 8:183–208.
- Brunel N, Hakim V (1999) Fast global oscillations in networks of integrate-and-fire neurons with low firing rates. *Neural Comput.* 11:1621–1671.
- Budd JM, Kisvárdy ZF (2001) Local lateral connectivity of inhibitory clutch cells in layer 4 of cat visual cortex (area 17). *Exp. Brain Res.* 140:245–250.
- Buzás P, Kovács K, Ferecskó AS, Budd JML, Eysel UT, Kisvárdy ZF (2006) Model-based analysis of excitatory lateral connections in the visual cortex. *J. Comp. Neurol.* 499:861–881.
- Buzsáki G, Anastassiou CA, Koch C (2012) The origin of extracellular fields and currents – EEG, ECoG, LFP and spikes. *Nat. Rev. Neurosci.* 13:407–427.
- Buzsáki G, Mizuseki K (2014) The log-dynamic brain: how skewed distributions affect network operations. *Nat. Rev. Neurosci.* 15:264–278.
- Buzsáki G, Wang XJ (2012) Mechanisms of gamma oscillations. *Annu. Rev. Neurosci.* 35:203–225.
- Cain N, Iyer R, Koch C, Mihalas S (2016) The computational properties of a simplified cortical column model. *PLoS Comput. Biol.* 12:e1005045.
- Camuñas Mesa LA, Quiroga RQ (2013) A detailed and fast model of extracellular recordings. *Neural Comput.* 25:1191–1212.
- Carnevale NT, Hines ML (2006) *The NEURON Book* Cambridge University Press, Cambridge.
- Chow CC, White JA, Ritt J, Kopell N (1998) Frequency Control in Synchronized Networks of Inhibitory Neurons. *J. Comput. Neurosci.* 5:407–420.
- Chu CCJ, Chien PF, Hung CP (2014a) Multi-electrode recordings of ongoing activity and responses to parametric stimuli in macaque V1. CRCNs.org .
- Chu CCJ, Chien PF, Hung CP (2014b) Tuning dissimilarity explains short distance decline of spontaneous spike correlation in macaque V1. *Vision Res.* 96:113–132.
- Contreras D, Destexhe A, Steriade M (1997) Intracellular and computational characterization of the intracortical inhibitory control of synchronized thalamic inputs in vivo. *J. Neurophysiol.* 78:335–350.
- Coombes S (2005) Waves, bumps, and patterns in neural field theories. *Biol. Cybern.* 93:91–108.
- De Schutter E, Van Geit W (2009) Modeling complex neurons In De Schutter E, editor, *Computational Modeling Methods for Neuroscientists*, chapter 11, pp. 260–283. MIT Press, Cambridge, MA, 1st edition.
- Denker M, Zehl L, Kilavik BE, Diesmann M, Brochier T, Riehle A, Grün S (2018) LFP beta amplitude is linked to mesoscopic spatio-temporal phase patterns. *Scientific Reports* 8:1–21.
- Destexhe A, Contreras D, Steriade M (1999) Spatiotemporal analysis of local field potentials and unit discharges in cat cerebral cortex during natural wake and sleep states. *J. Neurosci.* 19:4595–4608.
- Doiron B, Litwin-Kumar A, Rosenbaum R, Ocker GK, Josić K (2016) The mechanics of state-dependent neural correlations. *Nat. Neurosci.* 19:383–393.
- Douglas RJ, Martin KAC, Whitteridge D (1989) A canonical microcircuit for neocortex. *Neural Comput.* 1:480–488.
- Dubey A, Ray S (2016) Spatial spread of local field potential is band-pass in the primary visual cortex. *J. Neurophysiol.* 116:1986–1999.
- Ecker AS, Berens P, Keliris GA, Bethge M, Logothetis NK (2010) Decorrelated neuronal firing in cortical microcircuits. *Science* 327:584–587.
- Einevoll GT, Kayser C, Logothetis NK, Panzeri S (2013a) Modelling and analysis of local field potentials for studying the function of cortical circuits. *Nat. Rev. Neurosci.* 14:770–785.
- Einevoll GT, Lindén H, Tetzlaff T, Łęski S, Pettersen KH (2013b) Local field potentials: Biophysical origin and analysis In Quiroga RQ, Panzeri S, editors, *Principles of Neural Coding*, pp. 37–59. CRC Press.

- Einevoll GT, Pettersen KH, Devor A, Ulbert I, Halgren E, Dale AM (2007) Laminar population analysis: Estimating firing rates and evoked synaptic activity from multielectrode recordings in rat barrel cortex. *J. Neurophysiol.* 97:2174–2190.
- Ermentrout B (1998) Neural networks as spatio-temporal pattern-forming systems. *Reports on Progress in Physics* 61:353–430.
- Gewaltig MO, Diesmann M (2007) NEST (NEural Simulation Tool). *Scholarpedia* 2:1430.
- Gilbert CD, Wiesel TN (1989) Columnar specificity of intrinsic horizontal and corticocortical connections in cat visual cortex. *J. Neurosci.* 9:2432–2442.
- Grinvald A, Lieke EE, Frostig RD, Hildesheim R (1994) Cortical point-spread function and long-range lateral interactions revealed by real-time optical imaging of macaque monkey primary visual cortex. *J. Neurosci.* 14:2545–2568.
- Hadjipapas A, Lowet E, Roberts M, Peter A, Weerd PD (2015) Parametric variation of gamma frequency and power with luminance contrast: A comparative study of human MEG and monkey LFP and spike responses. *NeuroImage* 112:327–340.
- Hagen E, Dahmen D, Stavrinou ML, Lindén H, Tetzlaff T, van Albada SJ, Grün S, Diesmann M, Einevoll GT (2016) Hybrid scheme for modeling local field potentials from point-neuron networks. *Cereb. Cortex* 26:4461–4496.
- Hagen E, Næss S, Ness TV, Einevoll GT (2018) Multimodal modeling of neural network activity: computing LFP, ECoG, EEG and MEG signals with LFPy2.0. *bioRxiv* .
- Hagen E, Ness TV, Khosrowshahi A, Sørensen C, Fyhn M, Hafting T, Franke F, Einevoll GT (2015) ViSAPy: A python tool for biophysics-based generation of virtual spiking activity for evaluation of spike-sorting algorithms. *J. Neurosci. Meth.* 245:182–204.
- Hagen E, Senk J, van Albada SJ, Diesmann M (2016) Local field potentials in a 4x4mm² multi-layered network model In *25th Annual Computational Neuroscience Meeting: CNS-2016, BMC Neuroscience 2016, 17(Suppl 1):P167*.
- Hahne J, Dahmen D, Schuecker J, Frommer A, Bolten M, Helias M, Diesmann M (2017) Integration of continuous-time dynamics in a spiking neural network simulator. *Front. Neuroinformatics* 11:34.
- Hämäläinen M, Haari R, Ilmoniemi RJ, Knuutila J, Lounasmaa OV (1993) Magnetoencephalography — theory, instrumentation, and application to noninvasive studies of the working human brain. *Rev. Mod. Phys.* 65:413–496.
- Hao Y, Riehle A, Brochier TG (2016) Mapping horizontal spread of activity in monkey motor cortex using single pulse microstimulation. *Frontiers in neural circuits* 10:104.
- Hardingham NR, Larkman AU (1998) The reliability of excitatory synaptic transmission in slices of rat visual cortex in vitro is temperature dependent. *J. Physiol. (Lond.)* 507:249–256.
- Helias M, Tetzlaff T, Diesmann M (2014) The correlation structure of local cortical networks intrinsically results from recurrent dynamics. *PLoS Comput. Biol.* 10:e1003428.
- Hellwig B (2000) A quantitative analysis of the local connectivity between pyramidal neurons in layers 2/3 of the rat visual cortex. *Biol. Cybern.* 2:111–121.
- Herculano-Houzel S (2009) The human brain in numbers: a linearly scaled-up primate brain. *Front. Hum. Neurosci.* 3:31.
- Hill SL, Wang Y, Riachi I, Schürmann F, Markram H (2012) Statistical connectivity provides a sufficient foundation for specific functional connectivity in neocortical neural microcircuits. *Proc. Natl. Acad. Sci. USA* 109:E2885–E2894.
- Hines ML, Davison AP, Muller E (2009) NEURON and python. *Front. Neuroinformatics* 3:1.
- Hirsch JA, Gilbert CD (1991) Synaptic physiology of horizontal connections in the cat's visual cortex. *J. Neurosci.* 11:1800–1809.
- Holt GR, Koch C (1999) Electrical interactions via the extracellular potential near cell bodies. *J. Comput. Neurosci.* 6:169–184.
- Ian Nauhaus LB DLR, Carandini M (2012) Robustness of traveling waves in ongoing activity of visual cortex. *J. Neurosci.* 32:3088–3094.
- Izhikevich EM, Edelman GM (2008) Large-scale model of mammalian thalamocortical systems. *Proc. Natl. Acad. Sci. USA* 105:3593–3598.

- Jia X, Smith MA, Kohn A (2011) Stimulus selectivity and spatial coherence of gamma components of the local field potential. *J. Neurosci.* 31:9390–9403.
- Jia X, Tanabe S, Kohn A (2013a) Gamma and the coordination of spiking activity in early visual cortex. *Neuron* 77:762–774.
- Jia X, Xing D, Kohn A (2013b) No consistent relationship between gamma power and peak frequency in macaque primary visual cortex. *J. Neurosci.* 33:17–25.
- Jiang X, Shen S, Cadwell CR, Berens P, Sinz F, Ecker AS, Patel S, Tolias AS (2015) Principles of connectivity among morphologically defined cell types in adult neocortex. *Science* 350:aac9462–aac9462.
- Jordan J, Ippen T, Helias M, Kitayama I, Sato M, Igarashi J, Diesmann M, Kunkel S (2018) Extremely scalable spiking neuronal network simulation code: From laptops to exascale computers. *Front. Neuroinformatics* 12:2.
- Kajikawa Y, Schroeder CE (2011) How local is the local field potential? *Neuron* 72:847–858.
- Kandel ER, Markram H, Matthews PM, Yuste R, Koch C (2013) Neuroscience thinks big (and collaboratively). *Nat. Rev. Neurosci.* 14:659–664.
- Kang Y, Kaneko T, Ohishi H, Endo K, Araki T (1994) Spatiotemporally differential inhibition of pyramidal cells in the cat motor cortex. *J. Neurophysiol.* 71:280–293.
- Kasthuri N, Hayworth KJ, Berger DR, Schalek RL, Conchello JA, Knowles-Barley S, Lee D, Vázquez-Reina A, Kaynig V, Jones TR et al. (2015) Saturated reconstruction of a volume of neocortex 162:648–661.
- Katz B, Miledi R (1965) The effect of temperature on the synaptic delay at the neuromuscular junction. *J. Physiol. (Lond.)* 181:656–670.
- Kätzel D, Zemelman BV, Buetfering C, Wölfel M, Miesenböck G (2011) The columnar and laminar organization of inhibitory connections to neocortical excitatory cells. *Nat. Neurosci.* 14:100–107.
- Katzner S, Nauhaus I, Benucci A, Bonin V, Ringach DL, Carandini M (2009) Local origin of field potentials in visual cortex. *Neuron* 61:35–41.
- Keane A, Gong P (2015) Propagating waves can explain irregular neural dynamics. *J. Neurosci.* 35:1591–1605.
- Kisvárdy ZF, Eysel UT (1992) Cellular organization of reciprocal patchy networks in layer III of cat visual cortex (area 17). *Neuroscience* 46:275–286.
- Klein C, Evrard HC, Shapcott KA, Haverkamp S, Logothetis NK, Schmid MC (2016) Cell-targeted optogenetics and electrical microstimulation reveal the primate koniocellular projection to supra-granular visual cortex. *Neuron* 90:143–151.
- Kriener B, Helias M, Aertsen A, Rotter S (2009) Correlations in spiking neuronal networks with distance dependent connections. *J. Comput. Neurosci.* 27:177–200.
- Kriener B, Helias M, Rotter S, Diesmann M, Einevoll GT (2014) How pattern formation in ring networks of excitatory and inhibitory spiking neurons depends on the input current regime. *Front. Comput. Neurosci.* 7:1–21.
- Kunkel S, Morrison A, Weidel P, Eppler JM, Sinha A, Schenck W, Schmidt M, Vennemo SB, Jordan J, Peyser A, Plotnikov D, Graber S, Fardet T, Terhorst D, Mørk H, Trensch G, Seeholzer A, Deepu R, Hahne J, Blundell I, Ippen T, Schuecker J, Bos H, Diaz S, Hagen E, Mahmoudian S, Bachmann C, Lepperød ME, Breitwieser O, Golosio B, Rothe H, Setareh H, Djurfeldt M, Schumann T, Shusharin A, Garrido J, Muller EB, Rao A, Vieites JH, Plesser HE (2017) *Nest* 2.12.0.
- Laramée ME, Boire D (2015) Visual cortical areas of the mouse: comparison of parcellation and network structure with primates 8:149.
- Larkum ME, Zhu JJ, Sakmann B (2001) Dendritic mechanisms underlying the coupling of the dendritic with the axonal action potential initiation zone of adult rat layer 5 pyramidal neurons. *J. Physiol. (Lond.)* 533:447–466.
- Łęski S, Lindén H, Tetzlaff T, Pettersen KH, Einevoll GT (2013) Frequency dependence of signal power and spatial reach of the local field potential. *PLoS Comput. Biol.* 9:e1003137.
- Łęski S, Pettersen KH, Tunstall B, Einevoll GT, Gigg J, Wójcik DK (2011) Inverse current source density method in two dimensions: Inferring neural activation from multielectrode recordings. *Neuroinformatics* 9:401–425.

- Leung LS (1982) Nonlinear feedback model of neuronal populations in hippocampal CA1 region. *J. Neurophysiol.* 47:845–868.
- Levy RB, Reyes AD (2012) Spatial profile of excitatory and inhibitory synaptic connectivity in mouse primary auditory cortex. *J. Neurosci.* 32:5609–5619.
- Lindén H, Hagen E, Łęski S, Norheim ES, Pettersen KH, Einevoll GT (2014) LFPy: a tool for biophysical simulation of extracellular potentials generated by detailed model neurons. *Front. Neuroinformatics* 7:41.
- Lindén H, Pettersen KH, Einevoll GT (2010) Intrinsic dendritic filtering gives low-pass power spectra of local field potentials. *J. Comput. Neurosci.* 29:423–444.
- Lindén H, Tetzlaff T, Potjans TC, Pettersen KH, Grün S, Diesmann M, Einevoll GT (2011) Modeling the spatial reach of the LFP. *Neuron* 72:859–872.
- Livingstone MS, Hubel DH (1984) Specificity of intrinsic connections in primate primary visual cortex. *J. Neurosci.* 4:2830–2835.
- Lohmann H, Rörig B (1994) Long-range horizontal connections between supragranular pyramidal cells in the extrastriate visual cortex of the rat. *J. Comp. Neurol.* 344:543–558.
- Maier A, Adams GK, Aura C, Leopold DA (2010) Distinct superficial and deep laminar domains of activity in the visual cortex during rest and stimulation. *Front. Syst. Neurosci.* 4:31.
- Mainen ZF, Sejnowski TJ (1996) Influence of dendritic structure on firing pattern in model neocortical neurons. *Nature* 382:363–366.
- Markram H, Muller E, Ramaswamy S, Reimann MW, Abdellah M, Sanchez CA, Ailamaki A, Alonso-Nanclares L, Antille N, Arsever S, Kahou GAA, Berger TK, Bilgili A, Buncic N, Chalimourda A, Chindemi G, Courcol JD, Delalandre F, Delattre V, Druckmann S, Dumusc R, Dynes J, Eilemann S, Gal E, Gevaert ME, Ghobril JP, Gidon A, Graham JW, Gupta A, Haenel V, Hay E, Heinis T, Hernando JB, Hines M, Kanari L, Keller D, Kenyon J, Khazen G, Kim Y, King JG, Kisvarday Z, Kumbhar P, Lasserre S, Bé JVL, Magalhães BR, Merchán-Pérez A, Meystre J, Morrice BR, Muller J, Muñoz-Céspedes A, Muralidhar S, Muthurasa K, Nachbaur D, Newton TH, Nolte M, Ovcharenko A, Palacios J, Pastor L, Perin R, Ranjan R, Riachi I, Rodríguez JR, Riquelme JL, Rössert C, Sfyraakis K, Shi Y, Shillcock JC, Silberberg G, Silva R, Tauheed F, Telefont M, Toledo-Rodríguez M, Tränkler T, Geit WV, Díaz JV, Walker R, Wang Y, Zaninetta SM, DeFelipe J, Hill SL, Segev I, Schürmann F (2015) Reconstruction and simulation of neocortical microcircuitry. *Cell* 163:456–492.
- Martínez-Cañada P, Mobarhan MH, Halnes G, Fyhn M, Morillas C, Pelayo F, Einevoll GT (2018) Biophysical network modeling of the dLGN circuit: Effects of cortical feedback on spatial response properties of relay cells. *PLoS Comput. Biol.* 14:e1005930.
- Maynard EM, Nordhausen CT, Normann RA (1997) The Utah intracortical electrode array: A recording structure for potential brain-computer interfaces. *EEG Clin. Neurophysiol.* 102:228–239.
- McDonald CT, Burkhalter A (1993) Organisation of long-range inhibitory connections within rat visual cortex. *J. Neurosci.* 13:768–781.
- Mehring C, Hehl U, Kubo M, Diesmann M, Aertsen A (2003) Activity dynamics and propagation of synchronous spiking in locally connected random networks. *Biol. Cybern.* 88:395–408.
- Mitzdorf U (1985) Current source-density method and application in cat cerebral cortex: Investigation of evoked potentials and EEG phenomena. *Physiol. Rev.* 65:37–100.
- Mochizuki Y, Onaga T, Shimazaki H, Shimokawa T, Tsubo Y, Kimura R, Saiki A, Sakai Y, Isomura Y, Fujisawa S, Shibata KI, Hirai D, Furuta T, Kaneko T, Takahashi S, Nakazono T, Ishino S, Sakurai Y, Kitsukawa T, Lee JW, Lee H, Jung MW, Babul C, Maldonado PE, Takahashi K, Arce-McShane FI, Ross CF, Sessle BJ, Hatsopoulos NG, Brochier T, Riehle A, Chorley P, Grün S, Nishijo H, Ichihara-Takeda S, Funahashi S, Shima K, Mushiaki H, Yamane Y, Tamura H, Fujita I, Inaba N, Kawano K, Kurkin S, Fukushima K, Kurata K, Taira M, Tsutsui KI, Ogawa T, Komatsu H, Koida K, Toyama K, Richmond BJ, Shinomoto S (2016) Similarity in neuronal firing regimes across mammalian species. *J. Neurosci.* 36:5736–5747.
- Muller L, Chavane F, Reynolds J, Sejnowski TJ (2018) Cortical travelling waves: mechanisms and computational principles. *Nat. Rev. Neurosci.* 19:255–268.
- Muller L, Destexhe A (2012) Propagating waves in thalamus, cortex and the thalamocortical system: Experiments and models. *J. Physiol. (Paris)* 106:222–238.

- Muller L, Reynaud A, Chavane F, Destexhe A (2014) The stimulus-evoked population response in visual cortex of awake monkey is a propagating wave. *Nature Communications* 5.
- Murakoshi T, Guo JZ, Ichinose T (1993) Electrophysiological identification of horizontal synaptic connections in rat visual cortex in vitro. *Neuroscience Letters* 163:211–214.
- Nauhaus I, Busse L, Carandini M, Ringach DL (2009) Stimulus contrast modulates functional connectivity in visual cortex. *Nat. Neurosci.* 12:70–76.
- Nelson MJ, Pouget P (2010) Do electrode properties create a problem in interpreting local field potential recordings? *J. Neurophysiol.* 103:2315–2317.
- Nelson MJ, Pouget P, Nilsen EA, Patten CD, Schall JD (2008) Review of signal distortion through metal microelectrode recording circuits and filters 169:141–157.
- Ness TV, Chintaluri HC, Potworowski J, Łęski S, Głąbska H, Wójcik DK, Einevoll GT (2015) Modelling and analysis of electrical potentials recorded in multielectrode arrays (MEAs). *Neuroinformatics* 13:403–426.
- Nicholson C, Freeman JA (1975) Theory of current source-density analysis and determination of conductivity tensor for anuran cerebellum. *J. Neurophysiol.* 2:356–368.
- Nordlie E, Gewaltig MO, Plesser HE (2009) Towards reproducible descriptions of neuronal network models. *PLoS Comput. Biol.* 5:e1000456.
- Nunez PL, Srinivasan R (2006) *Electric Fields of the Brain, The Neurophysics of EEG* Oxford University Press, Inc., 2nd edition.
- Ohana O, Portner H, Martin KAC (2012) Fast recruitment of recurrent inhibition in the cat visual cortex. *PLoS ONE* 7:e40601.
- Ohki K, Reid RC (2007) Specificity and randomness in the visual cortex. *Curr. Opin. Neurobiol.* 17:401–407.
- Olavarria J, Sluyters RCV (1985) Unfolding and flattening the cortex of gyrencephalic brains. *J. Neurosci. Methods* 15:191–202.
- Packer AM, Yuste R (2011) Dense, unspecific connectivity of neocortical parvalbumin-positive interneurons: A canonical microcircuit for inhibition? *J. Neurosci.* 31:13260–13271.
- Pan WJ, Thompson GJ, Magnuson ME, Jaeger D, Keilholz S (2013) Infralow LFP correlates to resting-state fMRI BOLD signals. *NeuroImage* 74:288–297.
- Perin R, Berger TK, Markram H (2011) A synaptic organizing principle for cortical neuronal groups. *Proc. Natl. Acad. Sci. USA* 108:5419–5424.
- Perkel DH, Gerstein GL, Moore GP (1967) Neuronal spike trains and stochastic point processes. I. The single spike train. *Biophys. J.* 7:391–418.
- Petttersen KH, Devor A, Ulbert I, Dale AM, Einevoll GT (2006) Current-source density estimation based on inversion of electrostatic forward solution: Effects of finite extent of neuronal activity and conductivity discontinuities. *J. Neurosci. Methods* 154:116–133.
- Petttersen KH, Hagen E, Einevoll GT (2008) Estimation of population firing rates and current source densities from laminar electrode recordings. *J. Comput. Neurosci.* 24:291–313.
- Peyrache A, Dehghani N, Eskandar EN, Madsen JR, Anderson WS, Donoghue JA, Hochberg LR, Halgren E, Cash SS, Destexhe A (2012) Spatiotemporal dynamics of neocortical excitation and inhibition during human sleep. *Proc. Natl. Acad. Sci. USA* 109:1731–1736.
- Potjans TC, Diesmann M (2014) The cell-type specific cortical microcircuit: Relating structure and activity in a full-scale spiking network model. *Cereb. Cortex* 24:785–806.
- Potworowski J, Jakuczun W, Łęski S, Wójcik D (2012) Kernel current source density method. *NeuralComput* 24:541–575.
- Pyle R, Rosenbaum R (2017) Spatiotemporal dynamics and reliable computations in recurrent spiking neural networks 118.
- Quiroga RQ (2007) Spike sorting. *Scholarpedia* 2:3583.

- Ray S, Maunsell JHR (2010) Differences in gamma frequencies across visual cortex restrict their possible use in computation. *Neuron* 67:885–896.
- Ray S, Maunsell JHR (2011) Different Origins of Gamma Rhythm and High-Gamma Activity in Macaque Visual Cortex. *PLoS Comput. Biol.* 9:e1000610.
- Rees CL, Moradi K, Ascoli GA (2016) Weighing the evidence in Peters' rule: Does neuronal morphology predict connectivity? *Trends Neurosci.* 40:63–71.
- Reimann MW, Horlemann AL, Ramaswamy S, Muller EB, Markram H (2017) Morphological diversity strongly constrains synaptic connectivity and plasticity. *Cereb. Cortex* 27:4570–4585.
- Reimann MW, King JG, Muller EB, Ramaswamy S, Markram H (2015) An algorithm to predict the connectome of neural microcircuits. *Front. Comput. Neurosci.* 9:120.
- Renart A, De La Rocha J, Bartho P, Hollender L, Parga N, Reyes A, Harris KD (2010) The asynchronous state in cortical circuits. *Science* 327:587–590.
- Reyes-Puerta V, Yang JW, Siwek ME, Kilb W, Sun JJ, Luhmann HJ (2016) Propagation of spontaneous slow-wave activity across columns and layers of the adult rat barrel cortex in vivo. *Brain Structure Function* 221:4429–4449.
- Ribeiro PFM, Ventura-Antunes L, Gabi M, Mota B, Grinberg LT, Farfel JM, Ferretti-Rebustini REL, Leite REP, Filho WJ, Herculano-Houzel S (2013) The human cerebral cortex is neither one nor many: neuronal distribution reveals two quantitatively different zones in the gray matter, three in the white matter, and explains local variations in cortical folding 7:28.
- Riehle A, Wirtsohn S, Grün S, Brochier T (2013) Mapping the spatio-temporal structure of motor cortical lfp and spiking activities during reach-to-grasp movements. *Frontiers in Neural Circuits* 7:48.
- Robinson DA (1968) The electrical properties of metal microelectrodes. *Proceedings of the IEEE* 56:1065–1071.
- Rosenbaum R, Doiron B (2014) Balanced networks of spiking neurons with spatially dependent recurrent connections. *Physical Review X* 4:021039.
- Rosenbaum R, Smith MA, Kohn A, Rubin JE, Doiron B (2017) The spatial structure of correlated neuronal variability. *Nat. Neurosci.* 20:107–114.
- Rotter S, Diesmann M (1999) Exact digital simulation of time-invariant linear systems with applications to neuronal modeling. *Biol. Cybern.* 81:381–402.
- Roxin A, Brunel N, Hansel D (2005) The role of delays in shaping spatio-temporal dynamics of neuronal activity in large networks. *Phys. Rev. Lett.* 94:238103.
- Rubino D, Robbins KA, Hatsopoulos NG (2006) Propagating waves mediate information transfer in the motor cortex. *Nat. Neurosci.* 9:1549–1557.
- Sabatini BL, Regehr WG (1996) Timing of neurotransmission at fast synapses in the mammalian brain. *Nature* 384:170–172.
- Salin PA, Prince DA (1996) Electrophysiological mapping of GABAA receptor-mediated inhibition in adult rat somatosensory cortex. *J. Neurophysiol.* 75:1589–1600.
- Sato TK, Nauhaus I, Carandini M (2012) Traveling waves in visual cortex. *Neuron* 75:218–229.
- Schmidt M, Bakker R, Hilgetag CC, Diesmann M, van Albada SJ (2018) Multi-scale account of the network structure of macaque visual cortex. *Brain Structure & Function* 223:1409–1435.
- Schnepel P, Kumar A, Zohar M, Aertsen A, Boucsein C (2015) Physiology and impact of horizontal connections in rat neocortex. *Cereb. Cortex* 25:3818–3835.
- Schuecker J, Schmidt M, van Albada SJ, Diesmann M, Helias M (2017) Fundamental activity constraints lead to specific interpretations of the connectome. *PLoS Comput. Biol.* 13:e1005179.
- Schwalger T, Deger M, Gerstner W (2017) Towards a theory of cortical columns: From spiking neurons to interacting neural populations of finite size. *PLoS Comput. Biol.* 13:e1005507.
- Senk J, Hagen E, van Albada SJ, Diesmann M (2015) From randomly connected to spatially organized multi-layered cortical network models In *11th Göttingen Meeting of the German Neuroscience Society*.

- Senk J, Korvasová K, Schuecker J, Hagen E, Tetzlaff T, Diesmann M, Helias M (2018) Conditions for traveling waves in spiking neural networks. arXiv preprint arXiv:1801.06046v1 .
- Senk J, Yegenoglu A, Amblet O, Brukau Y, Davison A, Lester DR, Lührs A, Quaglio P, Rostami V, Rowley A, Schuller B, Stokes AB, van Albada SJ, Zielasko D, Diesmann M, Weyers B, Denker M, Grün S (2017) A collaborative simulation-analysis workflow for computational neuroscience using HPC. In Di Napoli E, Hermanns MA, Iliev H, Lintermann A, Peyser A, editors, *High-Performance Scientific Computing. JHPCS 2016. Lecture Notes in Computer Science, vol 10164.*, pp. 243–256.
- Sheng TK (1985) The distance between two random points in plane regions. *Adv. Appl. Prob.* 17:748–773.
- Shinomoto S, Shima K, Tanji J (2003) Differences in spiking patterns among cortical neurons. *Neural Comput.* 15:2823–2842.
- Smith MA, Jia X, Zandvakili A, Kohn A (2012) Laminar dependence of neuronal correlations in visual cortex. *J. Neurophysiol.* pp. 940–947.
- Smith MA, Kohn A (2008) Spatial and temporal scales of neuronal correlation in primary visual cortex. *J. Neurosci.* 28:12591–12603.
- Softky WR, Koch C (1993) The highly irregular firing of cortical cells is inconsistent with temporal integration of random EPSPs. *J. Neurosci.* 13:334–350.
- Sokol S (1976) Visually evoked potentials: Theory, techniques and clinical applications. *Survey of Ophthalmology* 21:18–44.
- Srinath R, Ray S (2014) Effect of amplitude correlations on coherence in the local field potential. *J. Neurophysiol.* 112:741–751.
- Stepanyants A, Hirsch JA, Martinez LM, Kisvárdy ZF, Ferecskó AS, Chklovskii DB (2008) Local potential connectivity in cat primary visual cortex. *Cereb. Cortex* 18:13–28.
- Stepanyants A, Martinez LM, Ferecskó AS, Kisvárdy ZF (2009) The fractions of short- and long-range connections in the visual cortex. *Proc. Natl. Acad. Sci. USA* 106:3555–3560.
- Swadlow HA, Gusev AG, Bezdudnaya T (2002) Activation of a cortical column by a thalamocortical impulse. *J. Neurosci.* 22:7766–7773.
- Takahashi K, Kim S, Coleman TP, Brown KA, Suminski AJ, Best MD, Hatsopoulos NG (2015) Large-scale spatiotemporal spike patterning consistent with wave propagation in motor cortex. *Nature Communications* 6.
- Tanigawa H, Wang Q, Fujita I (2005) Organization of horizontal axons in the inferior temporal cortex and primary visual cortex of the macaque monkey. *Cereb. Cortex* 15:1887–1899.
- Tetzlaff T, Helias M, Einevoll GT, Diesmann M (2012) Decorrelation of neural-network activity by inhibitory feedback. *PLoS Comput. Biol.* 8:e1002596.
- Tetzlaff T, Rotter S, Stark E, Abeles M, Aertsen A, Diesmann M (2008) Dependence of neuronal correlations on filter characteristics and marginal spike-train statistics. *Neural Comput.* 20:2133–2184.
- Thomson AM, West DC, Wang Y, Bannister AP (2002) Synaptic connections and small circuits involving excitatory and inhibitory neurons in layer 2-5 of adult rat and cat neocortex: Triple intracellular recordings and biocytin labelling in vitro. *Cereb. Cortex* 12:936–953.
- Thomson DJ (1982) Spectrum estimation and harmonic analysis. *Proc. IEEE* 70:1055–1096.
- Tomsett RJ, Ainsworth M, Thiele A, Sanayei M, Chen X, Gieselmann MA, Whittington MA, Cunningham MO, Kaiser M (2014) Virtual Electrode Recording Tool for EXtracellular potentials (VERTEX): comparing multi-electrode recordings from simulated and biological mammalian cortical tissue. *Brain Structure and Function* 220:2333–2353.
- Tusa RJ, Palmer LA, Rosenquist AC (1978) The retinotopic organization of area 17 (striate cortex) in the cat. *J. Comp. Neurol.* 177:213–235.
- van Albada SJ, Rowley AG, Senk J, Hopkins M, Schmidt M, Stokes AB, Lester DR, Diesmann M, Furber SB (2018) Performance comparison of the digital neuromorphic hardware SpiNNaker and the neural network simulation software NEST for a full-scale cortical microcircuit model. *Front. Neurosci.* 12:291.
- van Albada SJ, Helias M, Diesmann M (2015) Scalability of asynchronous networks is limited by one-to-one mapping between effective connectivity and correlations. *PLoS Comput. Biol.* 11:e1004490.

- van Essen DC, Maunsell JHR (1980) Two-dimensional maps of the cerebral cortex. *J. Comp. Neurol.* 191:255–281.
- van Kerkoerle T, Self MW, Dagnino B, Gariel-Mathis MA, Poort J, van der Togt C, Roelfsema PR (2014) Alpha and gamma oscillations characterize feedback and feedforward processing in monkey visual cortex. *Proc. Natl. Acad. Sci. USA* 111:14332–14341.
- Veit J, Hakim R, Jadi MP, Sejnowski TJ, Adesnik H (2017) Cortical gamma band synchronization through somato-statin interneurons. *Nat. Neurosci.* 20:951–959.
- Voges N, Perrinet L (2010) Phase space analysis of networks based on biologically realistic parameters. *J. Physiol. (Paris)* 104:51–60.
- Voges N, Perrinet L (2012) Complex dynamics in recurrent cortical networks based on spatially realistic connectivities. *Front. Comput. Neurosci.* 6:41.
- Voges N, Schüz A, Aertsen A, Rotter S (2010) A modeler's view on the spatial structure of intrinsic horizontal connectivity in the neocortex. *Prog. Neurobiol.* 92:277–292.
- Wagatsuma N, Potjans TC, Diesmann M, Fukai T (2011) Layer-dependent attentional processing by top-down signals in a visual cortical microcircuit model. *Front. Comput. Neurosci.* 5:31.
- Wang XJ, Buzsáki G (1996) Gamma Oscillation by Synaptic Inhibition in a Hippocampal Interneuronal Network Model. *J. Neurosci.* 16:6402–6413.
- Welch PD (1967) The use of fast fourier transform for the estimation of power spectra: A method based on time averaging over short, modified periodograms. *IEEE Transactions on Audio Electroacoustics* 15:70–73.
- Whittington MA, Traub RD, Kopell N, Ermentrout B, Buhl EH (2000) Inhibition-based rhythms: experimental and mathematical observations on network dynamics 38:315–336.
- Whittington MA, Traub RD, Jefferys JGR (1995) Synchronized oscillations in interneuron networks driven by metabotropic glutamate receptor activation. *Nature* 373:612–615.
- Wu JY, Huang X, Zhang C (2008) Propagating waves of activity in the neocortex: What they are, what they do. *The Neuroscientist* 14:487–502.
- Xing D, Yeh CI, Burns S, Shapley RM (2012) Laminar analysis of visually evoked activity in the primary visual cortex. *Proc. Natl. Acad. Sci. USA* 109:13871–13876.
- Xu W, Huang X, Takagaki K, young Wu J (2007) Compression and reflection of visually evoked cortical waves. *Neuron* 55:119–129.
- Yger P, El Boustani S, Destexhe A, Frégnac Y (2011) Topologically invariant macroscopic statistics in balanced networks of conductance-based integrate-and-fire neurons. *J. Comput. Neurosci.* 31:229–245.
- Zanos TP, Mineault PJ, Nasiotis KT, Guitton D, Pack CC (2015) A sensorimotor role for traveling waves in primate visual cortex. *Neuron* 85:615–627.